Robust Blind Deblurring Under Stripe Noise for Remote Sensing Images

Shuning Cao, Houzhang Fang, *Member, IEEE*, Liqun Chen, Wei Zhang, Yi Chang, *Member, IEEE*, and Luxin Yan, *Member, IEEE*

***Abstract*— The blind image deblurring methods have achieved great progress for Gaussian random noise. A few works have paid attention to image deblurring under structural noise, which is a very common degradation in multidetector imaging systems. This article considers the practical yet challenging problem of blind deblurring in the presence of the line-pattern stripe noise for remote sensing images. To overcome this issue, we explicitly formulate the structural noise into a novel and robust blind image deblurring framework. We observe that the structural line-pattern stripe noise would deteriorate both the kernel estimation and nonblind deblurring and propose a three-stage restoration framework to progressively estimate the blur kernel and clean image. Specifically, we first estimate an intermediate blur kernel by getting rid of the negative influence of the stripe noise in the unidirectional gradient domain. Next, a learning-based kernel refinement network is introduced to rectify the missing details of the inaccurate kernel. Finally, a low-rank decomposition-based nonblind deblurring model is proposed to simultaneously estimate the clean image and stripe noise. Experimental results on real and synthetic datasets demonstrate that the proposed robust blind image deblurring under stripe noise (RBDS) method outperforms the state-of-the-art blind deblurring methods.**

***Index Terms*— Blind deblurring, convolutional neural network (CNN), destriping, image restoration, low-rank representation.**

I. Introduction

REMOTE sensing images play a vital role in the Earth observation. However, the quality of acquired data is often affected by noise, blur, and other degradations [1]. Many works have been devoted to improving the image quality through image restoration methods [1], [2], [3], [4], [5]. The blur and stripe noise are very common degradations in remote sensing images. The image blur is mainly due to the fundamental limitation of the imaging system, the atmospheric effects, and the motion. The blurs would not only cause visual smoothness of the details but also weaken the discriminative features for high-level tasks. The blur procedure can be mathematically formulated as follows:

$$\boldsymbol{g} = \boldsymbol{h} \otimes \boldsymbol{o} + \boldsymbol{n} \tag{1}$$

where $\boldsymbol{g}$ is the observed blurry image, $\boldsymbol{o}$ is the clean image, $\otimes$ is the convolutional operator, $\boldsymbol{h}$ is the blur kernel, and $\boldsymbol{n}$ is assumed as random noise. The task of blind image deblurring is to recover the clean sharp image $\boldsymbol{o}$ along with the point spread function (PSF) $\boldsymbol{h}$ from the blurred image $\boldsymbol{g}$.

The structural line-pattern stripe noise is a very practical, common yet neglected artifact in various imaging systems, such as the remote sensing scanning systems [6] and the infrared focal plane array [7]. We provide a simplified illustration of the typical hyperspectral imaging procedure in Fig. 1. The hyperspectral image (HSI) is captured each time by a 2-D charge-coupled device (CCD) with one dimension for the scanned line restricted by the thin slit and the other dimension for the different wavelengths of the spectral signal via the diffraction grating. Thus, the nonuniform response of neighboring detectors due to the dark current generation, threshold variations, and gain or offset differences may unexpectedly generate the fixed-line-pattern stripe noise [8].

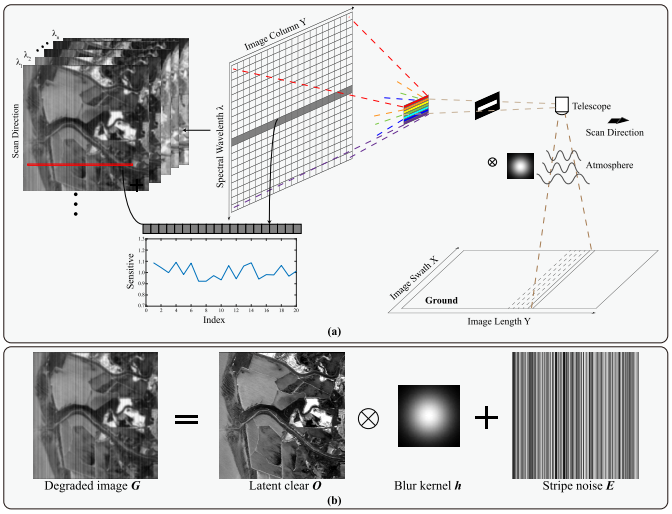


Fig. 1. Illustration of the blur and stripe noise degradation in the remote sensing image. (a) Imaging systems of a typical remote sensing HSI. On one hand, the disturbance of atmosphere would result in blurs. On the other hand, the nonuniform response of sensors leads to the stripe noise. (b) Mathematical formulation of the degradation process.

Manuscript received 17 June 2022; revised 30 July 2022; accepted 25 August 2022. Date of publication 29 August 2022; date of current version 7 October 2022. This work was supported in part by the National Natural Science Foundation of China under Grant 61971460, Grant 62101294, and Grant 41501371; and in part by JCJQ Program under Grant 2021-JCJQ-JJ-0060 *(Shuning Cao and Houzhang Fang contributed equally to this work.) (Corresponding author: Yi Chang.)*

Shuning Cao, Liqun Chen, Yi Chang, and Luxin Yan are with the National Key Laboratory of Science and Technology on Multispectral Information Processing, School of Artificial Intelligence and Automation, Huazhong University of Science and Technology, Wuhan 430074, China (e-mail: yichang@hust.edu.cn).

Houzhang Fang is with the School of Computer Science and Technology, Xidian University, Xi'an 710071, China.

Wei Zhang is with the Artificial Intelligence Center, Peng Cheng Laboratory, Shenzhen 518055, China.

Digital Object Identifier 10.1109/TGRS.2022.3202867

1558-0644 © 2022 IEEE. Personal use is permitted, but republication/redistribution requires IEEE permission.
See https://www.ieee.org/publications/rights/index.html for more information.

Authorized licensed use limited to: XIDIAN UNIVERSITY. Downloaded on November 24,2022 at 09:16:45 UTC from IEEE Xplore. Restrictions apply.

Recovering a sharp image from a single blurred photograph has long been a fundamental research problem and has made great progress in recent years [9], [10], [11], [12], [13], [14], [15], [16], [17], [18], [19], [20], [21]. Most of the existing deblurring methods mainly assume that the noise $\boldsymbol{n}$ is independent and identically distributed (i.i.d), such as the Gaussian or Poisson noise [22], [23]. However, this assumption is feasible for natural images but does not always hold for remote sensing images. In real blur cases, there exists a large category of non-i.i.d noises where the noises are spatially self-correlated and appear as regular structural patterns [24], [25], [26] in remote sensing images. In this work, we focus on a new task: blind image deblurring in presence of structural line-pattern stripe noise. To the best of our knowledge, very few works have paid attention to such a challenging yet important problem.

A natural and intuitive solution to this problem is to restore the clean image in a pipeline: removing the stripe noise first with a subsequent deblurring procedure. Although the destriping process could partially eliminate the stripe noise, the residual stripe will lead to amplified error in the final restoration. Moreover, the explicit stripe noise removal $\mathcal{R}(\cdot)$ would unexpectedly cause damage to the image details, which could be viewed as a low-pass filter operation on the degraded images as $\mathcal{R}(\boldsymbol{h} \otimes \boldsymbol{o})$, that is to say, the estimated kernel would be roughly approximated as two composite low-pass filters [22] and thus would significantly increase the difficulty of accurate blur kernel estimation. To overcome the problem, Chang *et al.* [27] proposed jointly destriping and deblurring within a unified optimization framework. However, they do not explicitly model the stripe noise and cannot fully get rid of the influence of the stripe for accurate kernel estimation. Moreover, the unified model is highly ill-posed with two unknown variables along with the stripe noise suppression, and the hyperparameters are tedious to choose.

In this work, we first propose a new blur and stripe degradation model, as shown in Fig. 1(b). Compared with the conventional blur model in (1), we further consider the stripe noise so that we can better model the influence of the stripe noise. We propose a three-phase image restoration framework that includes kernel initialization, kernel refinement, and nonblind deconvolution. Specifically, we utilize the directionality of the stripe noise to get rid of the negative influence of the stripe noise in the unidirectional gradient domain and propose a unidirectional variation optimization model to estimate a coarse kernel. Although the unidirectional gradient domain could benefit us to exclude the negative influence of the stripe noise, the lost image edges caused by the unidirectional operation would result in the estimated kernel being less accurate [28]. Next, we employ a simple data-driven learning convolutional neural network (CNN) to further rectify the estimated coarse kernel. Finally, we develop a low-rank decomposition-based nonblind deconvolution method to alternately perform image deblurring and destriping. Overall, the contributions can be summarized as follows.

1) *Task Formulation:* We focus on a new task: blind image deblurring under the stripe noise. A few works have been devoted to solving this challenging yet practical problem. Our work is the first to mathematically formulate the joint blur and stripe into a unified degradation model.
2) *Overall Framework:* We have provided a detailed analysis about the motivation and difficulty for this challenging task. Consequently, we formulate the blind image deblurring under stripe noise (RBDS) into a three-phase image restoration framework. Each stage is a very simpler subproblem with clear physical meaning: coarse kernel initialization, fine kernel estimation, and nonblind deconvolution with destriping.
3) *Kernel Estimation:* We propose a unidirectional variation optimization model to estimate the coarse kernel in the first stage and introduce a learning-based deep network to rectify the coarse kernel in the second stage. The joint physical model-driven optimization and data-driven learning network benefits us to better estimate the blur kernel, which inherits both the generalization and representation ability.
4) *Image Estimation:* We formulate the nonblind deblurring problem under stripe noise into a low-rank decomposition nonblind deconvolution model. The alternative image decomposition between stripe noise and clean image could gradually distinguish the clean image from stripe noise. Meanwhile, the blur and image are decoupled via deconvolution.
5) *Experimental Results:* The proposed method has been extensively validated on various datasets and significantly outperforms the state of the arts quantitatively and qualitatively. Besides, we show that the proposed method is robust to different image modalities and degradation levels.

We overview related work in Section II and then analyze the difficulty and the motivation of this work in Section III. Section IV presents the overall framework and each stage of the proposed method. The experimental results are described in Section V. Finally, the conclusion is given in Section VI.

II. Related Work

A. Remote Sensing Image Destriping

The stripe noise widely exists in various multidetector imaging systems, such as the HSIs [29], infrared focal plane array images [7], passive millimeter-wave (PMMW) [30], and medical images [31]. The previous methods can be roughly classified into three categories: filtering-based methods [32], [33], [34], optimization-based methods [6], [35], [36], [37], [38], [39], [40], [41], [42], and learning-based methods [8], [43], [44]. The filtering methods mainly suppress the specific frequency of the stripe noise in the transformed domain. Münch *et al.* [33] proposed a wavelet-fast Fourier transform (FFT) combined filter by performing Fourier shrinkage in stripe-related wavelet transformation subband. Although the stripe can be well suppressed, the image details with a similar frequency would be unexpectedly removed. Later, the optimization-based methods have dominated in the last decade by treating the destriping problem as an inverse problem with various sophisticated priors such as the Huber–Markov [6], unidirectional total variation (TV) [36], and low rank [38].

Authorized licensed use limited to: XIDIAN UNIVERSITY. Downloaded on November 24,2022 at 09:16:45 UTC from IEEE Xplore. Restrictions apply.

For example, Shen and Zhang [6] first presented the Huber–Markov prior to adaptively differing the stripe from the image details. The directionality of the stripe has been exploited to improve the representation of the stripes. Wang *et al.* [4] proposed an l_0 TV regularized low-rank tensor model for HSI mixed random and stripe noise removal. Most of the previous methods treat the destriping task as a noise removal problem. In this work, we formulate the stripe noise as the sparse error from the image decomposition perspective. Moreover, we tackle the stripe noise along with the image blurs, which is a more difficult and practical problem.

B. Remote Sensing Image Deblurring

The image deblurring methods have been extensively studied as a classical image processing problem [9], [10], [11], [12], [13], [14], [15], [16], [17], [18], [19], [20], [21]. According to whether the blur kernel is known in advance, the image deblurring can be classified into blind image deblurring and nonblind image deblurring. In this work, we focus on the blind image deblurring where the blur kernel is unknown.

The kernel estimation is crucial to blind deblurring. The image salient edges provide reliable cues for estimating blur kernel, while the texture and noise would mislead the kernel estimation [12]. There emerged tremendous great image priors to preserve the edges for kernel estimation, such as l_1 sparsity prior [16], l_1/l_2 prior [15], and unnatural l_0 sparsity prior [16]. Besides, Hu and Yang [45], [46] developed another line of work that measure and identify the suitable local regions of blurry images for kernel estimation. Recently, the deep learning-based methods have also achieved great progress for image deblurring [18], [19], [21], [47], [48], [49]. Most of them avoid the complex kernel estimation problem and directly predict the clean image. Tao *et al.* [21] proposed a scale-recurrent network (SRN) to produce a clean image end-to-end. The generative adversarial network (GAN) has been introduced to treat image deblurring as an image-to-image translation problem with an impressive visual appearance [49].

In this article, we mainly discuss single image deblurring methods [50], [51], [52], [53] for remote sensing and do not discuss HSI deblurring methods as they are another line of work. The blur in a remote sensing image is mainly due to the atmospheric effects and diffraction of the optical system [1], [54]. Zhang *et al*. [54] quantitatively analyzed the impact of blur kernel on the satellite image and suggested that the blur caused by PSF has a great impact on remote sensing imagery. Serre *et al.* [55] modeled the PSF of the ground-based space image as Moffat-Function, indicating that the PSF caused by atmospheric effects is Gaussian-like. For the image deblurring, Shen *et al.* [51] used the knife-edge features in remote sensing images to automatically detect salient edges for kernel estimation. Cao *et al.* [56] proposed an improved dark channel prior for blur kernel estimation, reaching a good deblurring performance on remote sensing images. Lim *et al* [52] proposed an l_0-norm-based intensity and dark channel prior for remote sensing images deblurring, and the proposed l_2-norm-based image fusion method further preserves the textures and details. Zhang *et al.* [53] discovered that find that local binary pattern (LBP) can record the texture features of the images and will not change by the blur. Therefore, they introduced an LBP prior and constructed the projected alternating minimization (PAM) algorithm to solve the model. Chang *et al.* [57] first proposed a unified optimization framework for multitask of remote sensing image restoration with low-rank tensor recovery theory. Most of these methods seldom consider the negative influence of noise on kernel estimation. In this work, we follow the classical two-phase stage framework [13], [14], [16] and extend it to a three-phase restoration framework with additional consideration of the stripe noise.

C. Learning-Based Remote Sensing Image Processing

Deep learning has been extensively studied in remote sensing community and great progress has been made in recent years for HSI processing/analysis [2], such as deep learning for multimodal classification [58], [59], [60], remote sensing image destriping [8], [44], and denoising [61], [62], [63], [64]. For example, Hong *et al.* [59] developed a new minibatch graph convolutional network (GCN) for HSI classification. Chang *et al.* [8] and Zhong *et al.* [44] introduced the CNN to well accommodate the complex distribution of the stripe due to its powerful nonlinear representation ability. Yuan *et al.* [62] proposed a deep combined spatial–spectral CNN HSI denoising. Although these learning-based methods have achieved great success, they have unexpectedly ignored the degradation procedure with strictly physical constraints. Thus, once there exists the domain gap between the training and test datasets, their performance would dramatically decrease due to the poor generalization of the learning-based methods. In this work, we combine the physical model-driven optimization and data-driven learning network to jointly estimate the blur kernel, which inherits both the generalization and the representation ability.

III. Analysis of Difficulty and Observations

In this section, we first analyze the difficulty of this challenging task. Then, we analyze how the stripe noise influent the blind deblurring in terms of both kernel estimation and nonblind image restoration. Finally, we show the key property of the stripe to get rid of its influence on the stripe.

A. Difficulty of Blind Deblurring Under Stripe Noise

Given the degraded image $\boldsymbol{g}$, the goal of this work is to estimate the clean image $\boldsymbol{o}$, blur kernel $\boldsymbol{h}$, and also the stripe noise $\boldsymbol{e}$. In previous image deblurring tasks, the nonblind deblurring problem assumes that the blur kernel $\boldsymbol{h}$ is known in advance, which significantly reduces the difficulty since it only needs to estimate the clean image $\boldsymbol{o}$. Then, the blind deblurring problem needs to estimate both $\boldsymbol{h}$ and $\boldsymbol{o}$ in which the task is more ill-posed. Later, the researchers begin to consider a more realistic situation: blind image deblurring in the presence of noise where the random noise $\boldsymbol{n}$ is involved. The noise would dramatically influence the blur kernel estimation. Here, we focus on a more realistic situation in remote sensing

Authorized licensed use limited to: XIDIAN UNIVERSITY. Downloaded on November 24,2022 at 09:16:45 UTC from IEEE Xplore. Restrictions apply.

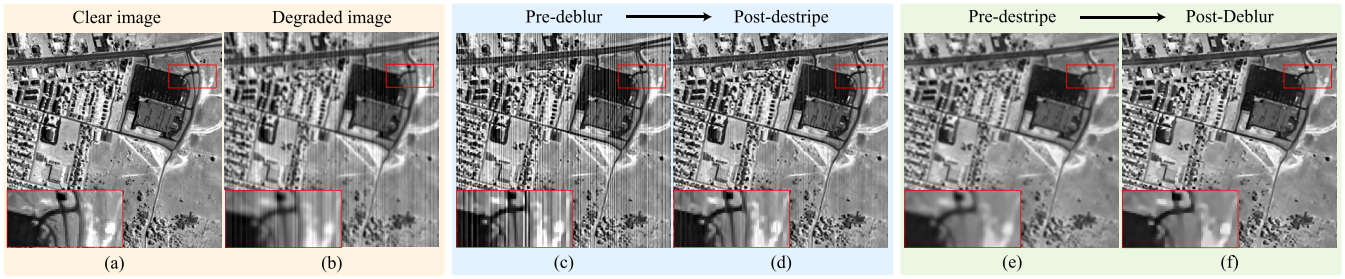


Fig. 2. Illustration of the difficulty of the image with both blur and stripe. (a) and (b) Clean and degraded images. Two different restoration pipelines are employed for illustration. (c) and (d) Deblurring first with subsequent destriping, which leaves an obvious residual stripe. (e) and (f) Destriping first with subsequent deblurring, which clearly oversmooth the details.

images, and not only the random noise but also the stripe noise are involved; meanwhile, the blur kernel is also unknown. Imaging that, given only one variable $\boldsymbol{g}$, three unknown variables need to be estimated, which is a very difficult task.

Moreover, the destriping and deblurring procedures are inherently contradictory to each other, which makes the RBDS a very difficult problem. The definition of image deblurring is to recover a sharp image $\boldsymbol{o}$ from a blurred image $\boldsymbol{g}$, that is to say, the image deblurring is to retrieve the high-frequency image edges from the smoothed low-frequency component. On the contrary, the image destriping is to remove the high-frequency line-pattern structures $\boldsymbol{e}$ from the degraded images $\boldsymbol{g}$.

To illustrate this, we synthesize a blurred and striped image via (4) and perform the destriping and deblurring successively,[1] and vice versa, as shown in Fig. 2. Directly applying the deblurring would partially recover the image details but at the expense of significantly enhanced striping artifacts [Fig. 2(c)]. On the contrary, although destriping could well suppress the stripe noise, the image details would be inevitably damaged at the same time [Fig. 2(e)]. It suggests that destriping and deblurring are mutually exclusive to each other. Moreover, in Fig. 2(d) and (f), we perform the complementary destriping and deblurring procedure of Fig. 2(c) and (e), respectively. In Fig. 2(d), the stripe noise is difficult to be satisfactorily removed because the stripe noise has been unexpectedly enhanced by deblurring. In Fig. 2(f), the image details cannot be ideally recovered since the image details have been inevitably suppressed by destriping.

Thus, we have one key observation: the deblurring and destriping cannot be handled separately and should be tightly coupled. In this work, we do not jointly perform blind deblurring and destriping as in [27]. Instead, we follow the two-phase blind image deblurring framework with blur kernel estimation and nonblind image deblurring. Thus, compared with [27], our framework employs the nonblind deblurring and destriping, which could significantly reduce the optimization difficulty with fewer variables to be estimated.

B. Influence of Stripe Noise on Blind Deblurring

Blind image deblurring consists of two important steps: kernel estimation and nonblind image deblurring. Here, we provide a detailed analysis of how the stripe noise would heavily influence both two steps.

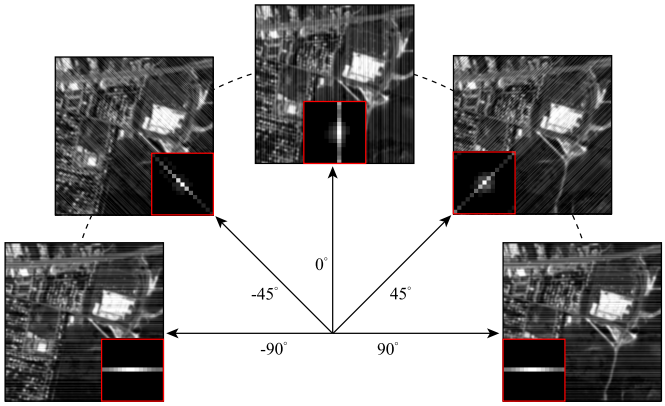


Fig. 3. Influence of stripe noise on kernel estimation. We manually synthesize the stripe noise with different angles $\{-90°, -45°, 0°, 45°, 90°\}$ on the blurred image. Interestingly, the estimated kernels consistently possess similar direction and shape as the corresponding stripe noises.

On the one hand, the stripe noise would severely affect the kernel estimation accuracy for its line-pattern structural property, as shown in Fig. 3. To analyze how the stripe would influence the blur kernel estimation, we manually synthesize the stripe noise with different angles $\{-90°, -45°, 0°, 45°, 90°\}$ on the blurred image. We estimate the blur kernel in the gradient space as the method of [65]. Interestingly, we can observe that the estimated kernels consistently possess similar direction and shape as the corresponding stripe noises. It is widely accepted that the kernel estimation is to retrieve the "cue" from the saliency edges of the degraded images. Unfortunately, the stripe noises possess strong structures, which are visually similar to the saliency image edges. Such an ambiguity between the stripe noise and image edges would mislead the kernel estimation, as shown in Fig. 3. On the other hand, given the blur kernel, the stripe noise would also be unexpectedly enhanced during the nonblind image deblurring procedure. In Fig. 2(c), we can observe that the striping artifacts are even more obvious after the deblurring procedure. This is reasonable since the deblurring algorithm has mistakenly regarded the line-pattern stripe noise as the image edges to be recovered.

We can conclude that the stripe noise would affect both the kernel estimation and the nonblind image deblurring procedure. We argue that the fundamental problem of this task lies in

[1]We employ SOTA RGTV [65] for deblurring and SGE [35] for destriping.

Authorized licensed use limited to: XIDIAN UNIVERSITY. Downloaded on November 24,2022 at 09:16:45 UTC from IEEE Xplore. Restrictions apply.

distinguishing the stripe noise and image details. Our starting point is to exclude the negative influence of the stripe, which is similar to the outlier blind deblurring [25], [26], [66], [67]. Thus, the task of RBDS is to excavate the intrinsic property of stripe noise, excluding the negative influence of the stripe in each step.

C. Key Property of Stripe Noise

The property of stripe noise has been extensively studied in the destriping field. The directionality is the key property of the line-pattern stripe noise. The directionality is inherently determined by the imaging principle of the multidetector system. In this work, we introduce two widely adopt domains to model the directionality: gradient domain-based smoothness [36] and sparsity domain-based low rankness [38].

Property 1: The smoothness has been widely utilized in unidirectional variational models [36], where they assume that the stripe noise has significantly changed the gradient across the stripe and has little influence on the gradient along the stripe. We mathematically formulate this property as

$$\nabla_x \boldsymbol{E} \gg \nabla_y \boldsymbol{E} \approx 0 \tag{2}$$

where x and y denote the horizontal and vertical directions, respectively.[2] The rationality behind (2) is that we assume that in a very short scanning period for a scene, the variance of the systematic error of each detector is very small.

Property 2: The low rankness has been widely utilized in low-rank recovery models [38], where they assume that the stripe noise has distinct low-rank property

$$\operatorname{rank}(\boldsymbol{E}) \leq r. \tag{3}$$

The rationality behind (3) is the self-similarity of the stripe noise along both the x- and y-directions. On one hand, the systematic error of each detector is almost consistent along the stripe direction, which means that the row rank is very small. On the other hand, across the stripe direction, each stripe line is very similar to the other with regular line patterns, which means that the column rank is also very small.

Note that, in this work, our contribution is not the discovery of the property of the stripe, but how to sophisticatedly utilize these properties in blind striped image deblurring tasks. The interested readers about the properties could refer to [36] and [38] for more details.

IV. Proposed Approach

A. Unified Stripe and Blur Degradation Model

The conventional blur model ($\boldsymbol{g} = \boldsymbol{h} \otimes \boldsymbol{o} + \boldsymbol{n}$) often assumes that noise $\boldsymbol{n}$ to be random and i.i.d. Unfortunately, its performance and applicability in real scenarios are limited by a lack of robustness to outlying or corrupted observations, such as the typical case of line-pattern stripe noise in remote sensing images. We formulate the line-pattern stripe as the structural sparse error $\boldsymbol{e}$ and distinguish from nonstructural noise $\boldsymbol{n}$. The conventional blur model (1) is extended to a novel robust blind image deblurring model

$$\boldsymbol{g} = \boldsymbol{o} \otimes \boldsymbol{h} + \boldsymbol{e} + \boldsymbol{n} \tag{4}$$

to accommodate the stripe noise and blur simultaneously. This novel model explicitly formulates the structural and non-i.i.d stripe noise as the gross error $\boldsymbol{e}$. The word "robust" is first used in classical work robust principal component analysis (RPCA) [68], where the corrupted entries $\boldsymbol{e}$ are unknown and the errors can be arbitrarily large (modeling grossly corrupted observations common in visual and bioinformatic data) but are assumed to be sparse. Thus, the "robust" in "robust blind deblurring" means that the proposed method robust RBDS is very robust to stripe noise for the blind deblurring task.

B. Framework of the Proposed Method

In this work, we follow the classical two-phase framework [14], kernel estimation and nonblind deblurring, and extend it to the three-step paradigm, as shown in Fig. 4. We argue that the key to the RBDS is to accurately estimate the blur kernel by getting rid of the influence of the stripe. Different from the outlier blind deblurring method [66] which is to exclude the outliers to avoid the influence of the outlier on the blur kernel estimation, the proposed blind deblurring method under stripe is to recover the stripe regions to further exploit more informative regions for better blur kernel estimation. In the kernel estimation, we first utilize Property 1 to estimate the kernel in the unidirectional (along the stripe) gradient domain to exclude the influence of the stripe noise. However, the unidirectional operation would also result in the loss of the useful image edges along this direction. Thus, the estimated kernel in the first step needs to be further refined. In the second step, we formulate the kernel refinement task as a regression task by introducing a simple CNN to rectify the inaccurate kernel. Once the kernel has been well estimated, the problem can be reduced to a tractable nonblind deblurring in the presence of stripe noise. We utilize the low-rank property in Property 2 to model the stripe noise and develop a low-rank decomposition-based deblurring model to alternately estimate the clean image and stripe component, namely, joint nonblind deblurring and destriping.

C. Stage One: Unidirectional Kernel Estimation

The kernel estimation in a classical two-phase blind deblurring method is usually performed in the isotropic gradient domain

$$\min_{\nabla \boldsymbol{o}, \boldsymbol{h}} \|\nabla \boldsymbol{g} - \boldsymbol{h} \otimes \nabla \boldsymbol{o}\|_2^2 + \gamma P_h(\boldsymbol{h}) + \lambda P_o(\nabla \boldsymbol{o}) \tag{5}$$

where $\nabla = (\nabla_x, \nabla_y)^T$ denotes the derivative along both the x- and y-directions, and P_o and P_h are the priors for the image and kernel, respectively. However, due to the stripe noise, (5) is not applicable anymore. In Fig. 5, we simulate the degraded image with the standard Gaussian kernel. From left to right, the first row shows the salient image edges $\nabla \boldsymbol{o}$ of different scales and also the estimated kernel $\boldsymbol{h}$ via (5). We can observe that the salient image edges contain obvious stripe

[2] In this work, we assume that the direction of the stripes is all vertical.

Authorized licensed use limited to: XIDIAN UNIVERSITY. Downloaded on November 24,2022 at 09:16:45 UTC from IEEE Xplore. Restrictions apply.

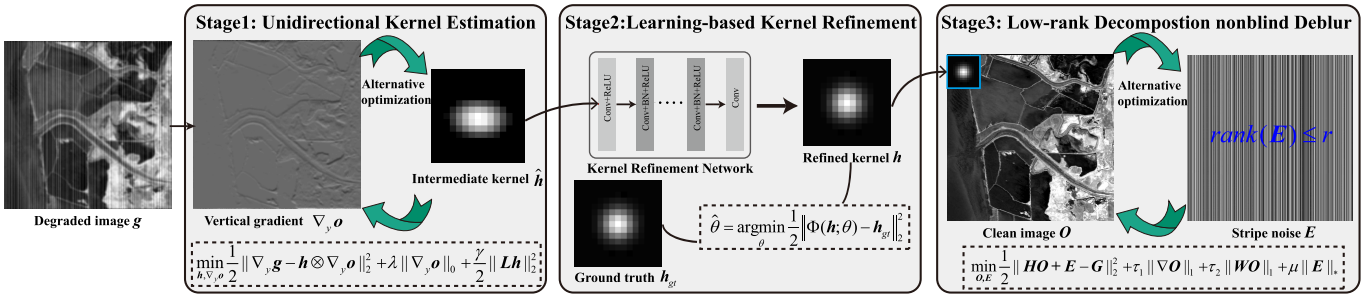


Fig. 4. Framework of the three-phase RBDS. First, we estimate the inaccurate blur kernel within the unidirectional gradient domain with Property 1, which eliminates the disturbance of stripe noise to kernel estimation. Then, we refine the estimated kernel by the kernel refinement network, to rectify the inaccurate kernel due to the lost information in the unidirectional gradient domain. Finally, we propose a low-rank decomposition-based nonblind deconvolution model to alternatively perform nonblind deblurring and destriping.

artifacts, which have been mistakenly regarded as the useful large edges for kernel estimation. This is the main reason why the estimated kernel also possesses the similar pattern as the stripe noise.

Existing blind deblurring methods usually estimate blur kernel in the gradient domain by isotropically utilizing both the horizontal and the vertical gradient. This is reasonable if the image merely contains random noise. As for the stripe noise, we employ the new degradation model (4) to take the stripe noise into consideration. The analysis in Section III-B motivates us to eliminate the stripe noise in the intermediate edges map for kernel estimation. Specifically, we unfold the derivative operation $\nabla = (\nabla_x, \nabla_y)^T$ in (5) into two terms

$$\min_{\nabla_x \boldsymbol{o}, \boldsymbol{h}} \|\nabla_x \boldsymbol{g} - \boldsymbol{h} \otimes \nabla_x \boldsymbol{o} - \nabla_x \boldsymbol{e}\|_2^2 + \gamma\, P_h(\boldsymbol{h}) + \lambda P_o(\nabla_x \boldsymbol{o}) \quad (6a)$$

$$\min_{\nabla_y \boldsymbol{o}, \boldsymbol{h}} \left\|\nabla_y \boldsymbol{g} - \boldsymbol{h} \otimes \nabla_y \boldsymbol{o} - \nabla_y \boldsymbol{e}\right\|_2^2 + \gamma\, P_h(\boldsymbol{h}) + \lambda P_o(\nabla_y \boldsymbol{o}). \quad (6b)$$

The two terms in (6) denote the kernel $\boldsymbol{h}$ estimated from the horizontal and vertical gradient domains. Note that, in Section III-C, we have shown that the vertical gradient of stripe noise $\nabla_y \boldsymbol{e} \approx 0$, which means that we can exclude the stripe in the vertical gradient domain. Then, we have

$$\min_{\nabla_x \boldsymbol{o}, \boldsymbol{h}} \|\nabla_x \boldsymbol{g} - \boldsymbol{h} \otimes \nabla_x \boldsymbol{o} - \nabla_x \boldsymbol{e}\|_2^2 + \gamma\, P_h(\boldsymbol{h}) + \lambda P_o(\nabla_x \boldsymbol{o}) \quad (7a)$$

$$\min_{\nabla_y \boldsymbol{o}, \boldsymbol{h}} \left\|\nabla_y \boldsymbol{g} - \boldsymbol{h} \otimes \nabla_y \boldsymbol{o}\right\|_2^2 + \gamma\, P_h(\boldsymbol{h}) + \lambda P_o(\nabla_y \boldsymbol{o}). \quad (7b)$$

Thus, we can solve (7b) following the general gradient-based kernel estimation strategy since we have mostly eliminated the stripe noise $\boldsymbol{e}$. In Fig. 5, the second and third row show the kernel estimated by only the horizontal gradient (7a) and vertical gradient (7b) domain, respectively. We can observe that the salient image edges of the purely horizontal gradient domain contain even more server stripe artifacts, leading to more thinner kernel. On the contrary, the salient image edges of the purely vertical gradient domain do not contain any stripe artifacts, leading to an approximate Gaussian kernel.

These results strongly support the effectiveness of the anisotropic vertical gradient domain (along the stripe) for kernel estimation. Thus, we can specialize (7b) with the concrete unidirectional gradient kernel estimation model

$$\min_{\boldsymbol{h}, \nabla_y \boldsymbol{o}} \frac{1}{2}\left\|\nabla_y \boldsymbol{g} - \boldsymbol{h} \otimes \nabla_y \boldsymbol{o}\right\|_2^2 + \lambda \left\|\nabla_y \boldsymbol{o}\right\|_0 + \frac{\gamma}{2}\|\boldsymbol{L}\boldsymbol{h}\|_2^2 \quad (8)$$

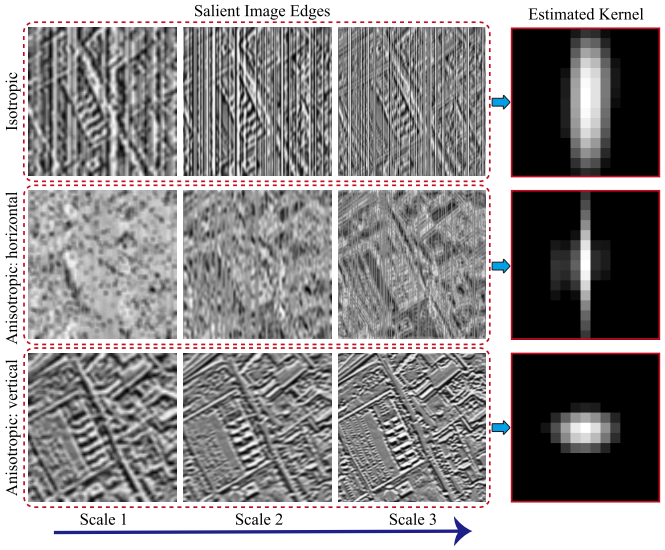


Fig. 5. Comparison between the anisotropic and isotropic gradient domain for kernel estimation. (From Left to Right) Each row shows the estimated intermediate gradient image maps and also the blur kernel. (From Top to Bottom) We show three different ways to select the sharp edges: isotropic gradient, anisotropic horizontal gradient, and anisotropic vertical gradient.

where the image prior is regularized with l_0 for better edge selection. As for the kernel, the simultaneous autoregressive (SAR) model $\|\boldsymbol{L}\boldsymbol{h}\|_2^2$ is employed, which is very suitable for the smooth PSF [69]. The combination of Laplacian operator $\boldsymbol{L}$ and the L_2-norm regularizes the blur kernel estimation $\boldsymbol{h}$ to be smooth. In multidetector systems, we assume that the blur kernel is usually a Gaussian blur. Due to the difficulty of estimating multiple variables directly, we adopt the alternating minimization scheme to solve the objective functional (8) with respect to the unidirectional image edges $\nabla_y \boldsymbol{o}$ and blur kernel $\boldsymbol{h}$.

1) Blur Kernel $\boldsymbol{h}$ Estimation: With $\nabla_y \boldsymbol{o}$ fixed, (8) can be relaxed to the least-square problem

$$\boldsymbol{h} = \arg\min_{\boldsymbol{h}} \frac{1}{2}\left\|\boldsymbol{h} \otimes \nabla_y \boldsymbol{o} - \nabla_y \boldsymbol{g}\right\|_2^2 + \frac{\gamma}{2}\|\boldsymbol{L}\boldsymbol{h}\|_2^2 \quad (9)$$

which can be fastly solved in FFT

$$\boldsymbol{h} = \mathcal{F}^{-1}\left(\frac{\overline{\mathcal{F}}(\nabla_y \boldsymbol{o}) \cdot \mathcal{F}(\nabla_y \boldsymbol{g})}{\overline{\mathcal{F}}(\nabla_y \boldsymbol{o}) \cdot \mathcal{F}(\nabla_y \boldsymbol{o}) + \gamma\, \overline{\mathcal{F}}(\boldsymbol{L}) \cdot \mathcal{F}(\boldsymbol{L})}\right) \quad (10)$$

Authorized licensed use limited to: XIDIAN UNIVERSITY. Downloaded on November 24,2022 at 09:16:45 UTC from IEEE Xplore. Restrictions apply.

where $\mathcal{F}$ denotes the 2-D FFT operator, $\overline{\mathcal{F}}$ is the complex conjugate, and $\mathcal{F}^{-1}$ is the inverse FFT.

2) Image Edges $\nabla_y \boldsymbol{o}$ Estimation: With $\boldsymbol{h}$ fixed, (8) can be reduced to the following problem:

$$\nabla_y \boldsymbol{o} = \arg\min_{\nabla_y \boldsymbol{o}} \frac{1}{2}\left\|\boldsymbol{h} \otimes \nabla_y \boldsymbol{o} - \nabla_y \boldsymbol{g}\right\|_2^2 + \lambda \left\|\nabla_y \boldsymbol{o}\right\|_0. \quad (11)$$

Since the l_0-norm is nondifferentiable, we introduce the splitting Bregman iteration [70] to solve (11). The main idea is to introduce an auxiliary variable $\boldsymbol{p} = \nabla_y \boldsymbol{o}$

$$\min_{\nabla_y \boldsymbol{o}, \boldsymbol{p}} \lambda \|\boldsymbol{p}\|_0 + \frac{\beta}{2}\|\boldsymbol{p} - \nabla_y \boldsymbol{o} - \boldsymbol{v}\|_2^2 + \frac{1}{2}\left\|\boldsymbol{h} \otimes \nabla_y \boldsymbol{o} - \nabla_y \boldsymbol{g}\right\|_2^2 \quad (12)$$

where β denotes the Bregman penalization parameters and $\boldsymbol{v}$ is the Bregman iteration variable. Similarly, (12) can be the equivalence of two subproblems

$$\nabla_y \boldsymbol{o} = \arg\min_{\nabla_y \boldsymbol{o}} \frac{\beta}{2}\left\|\boldsymbol{p} - \nabla_y \boldsymbol{o} - \boldsymbol{v}\right\|_2^2 + \frac{1}{2}\left\|\boldsymbol{h} \otimes \nabla_y \boldsymbol{o} - \nabla_y \boldsymbol{g}\right\|_2^2 \quad (13)$$

$$\boldsymbol{p} = \arg\min_{\boldsymbol{p}} \lambda \|\boldsymbol{p}\|_0 + \frac{\beta}{2}\left\|\boldsymbol{p} - \nabla_y \boldsymbol{o} - \boldsymbol{v}\right\|_2^2. \quad (14)$$

The closed-form solution of (13) can be obtained

$$\nabla_y \boldsymbol{o} = \mathcal{F}^{-1}\left(\frac{\beta \mathcal{F}(\boldsymbol{p} - \boldsymbol{v}) + \overline{\mathcal{F}}(\boldsymbol{h}) \cdot \mathcal{F}(\nabla_y \boldsymbol{g})}{\overline{\mathcal{F}}(\boldsymbol{h})\mathcal{F}(\boldsymbol{h}) + \beta}\right). \quad (15)$$

The closed-form solution of $\boldsymbol{p}$ can be obtained by hard-threshold shrinkage [71]

$$\boldsymbol{p} = \begin{cases} 0, & (\nabla_y \boldsymbol{o} + \boldsymbol{v})^2 \le 2\lambda/\beta \\ \nabla_y \boldsymbol{o} + \boldsymbol{v}, & \text{otherwise.} \end{cases} \quad (16)$$

The Bregman variable $\boldsymbol{v}$ is updated by

$$\boldsymbol{v}^{t+1} = \boldsymbol{v}^t + \nabla_y \boldsymbol{o} - \boldsymbol{p}. \quad (17)$$

The kernel estimation process is summarized in Algorithm 1.

Algorithm 1 Unidirectional Kernel Estimation

Require: Image pyramid of input image $\boldsymbol{g}$: $\{\boldsymbol{g}_0, \boldsymbol{g}_1, \ldots, \boldsymbol{g}_S,\}$
Initialize: λ, γ; $\boldsymbol{v}^1 = 0$; $S = 3$, $N = 5$; $\nabla_y \boldsymbol{o}^1 = \nabla_y \boldsymbol{g}$
for $s = 1$ to S **do**
  for $i = 0$ to N **do**
    Kernel Estimation: Estimate $\boldsymbol{h}^{i+1}$ by Eq. (10);
    for $t = 0$ to T **do**
      Sharp Edge: Solve $\nabla_y \boldsymbol{o}^{t+1}$ via Eq. (15);
      Auxiliary Variable: Solve $\boldsymbol{p}^{t+1}$ via Eq. (16);
      Bregman Iteration: Update $\boldsymbol{v}^{t+1}$ via Eq. (17);
    end for
  end for
end for
Ensure: Coarse blur kernel $\hat{\boldsymbol{h}}$.

D. Stage Two: Learning-Based Inaccurate Kernel Refinement

In stage one, to get rid of the stripe noise, we estimate the blur kernel in the unidirectional gradient domain along the stripe. Although the stripe noise can be eliminated in the unidirectional domain, the image structures of the direction along the stripe are also losing. Consequently, the estimated blur kernel could only retrieve the "cues" from the unidirectional gradient across the stripe. This is the main reason why the estimated kernel in the third row of Fig. 5 is an ellipse with transverse dominance. Thus, the goal of stage two is to rectify the inaccurate kernel in the first stage.

The inaccurate kernel refinement has been explored by previous methods, where they usually correct the kernel uncertainty [72] by imposing handcrafted sparse prior to recover the deconvolution error. However, the linear transformation of the optimization model may not suitable for the complex refinement procedure. In this work, we formulate the inaccurate kernel refinement task as a learning-based regression problem. We introduce a simple deep residual CNN [73] to learn the kernel error between the GT kernel and the inaccurate kernel estimation. The advantages are two folds. First, the CNN possesses a powerful nonlinear representation ability, which makes it more suitable for unknown and complex recovery tasks. Second, the residual learned by the network is exactly the error between the input kernel and the output kernel, which makes it very suitable for training.

Note that, we do not directly learn the blur kernel or the clean image. The first stage model-driven optimization method has a clear physical meaning, and the second stage data-driven learning method has good representation ability endowed by the CNN. Thus, the proposed method could achieve a good balance in terms of the physical meaning and representation for blur kernel estimation. Compared with directly learning for the kernel [47], our coarse-to-fine strategy would provide a very good initialization for the blur kernel, which significantly eases the learning difficulty. Moreover, end-to-end learning would completely ignore the physical degradation mechanism. On the other hand, compared with directly learning for the clean image [21], the blur kernel is much smaller with less variance, which makes it much easier to be learned.

We simulate the Gaussian kernels with the variance from 1.1 to 2.1 with the interval 0.1, and the stripe noise with the intensities randomly varies from $[-30, 30]$. Then, we randomly select 5000 Place2 images [74] with the size 256×256 for simulation. Most of the blur and stripe in a real multidetector imaging system are covered by the simulation. In total, we have 600 000 samples with different degrees of stripe and blur for training. We use Algorithm 1 to generate the inaccurate blur kernel as the input $\hat{\boldsymbol{h}}$, and the ground-truth blur kernel $\boldsymbol{h}_{gt}$ is set as the output for training. The network is trained in a supervised way

$$\hat{\theta} = \arg\min_{\theta} \frac{1}{2}\left\|\Phi(\hat{\boldsymbol{h}}; \theta) - \boldsymbol{h}_{gt}\right\|_2^2 \quad (18)$$

where Φ and θ are the learned mappings and the learned parameters of the kernel refine network, respectively. Note that, the network architecture is not the key point of this work. We employ the DnCNN [73] as our refinement network, which outperforms the U-Net and ResNet on kernel refinement by our implementation, Fig. 6 presents the comparison between them.

Authorized licensed use limited to: XIDIAN UNIVERSITY. Downloaded on November 24,2022 at 09:16:45 UTC from IEEE Xplore. Restrictions apply.

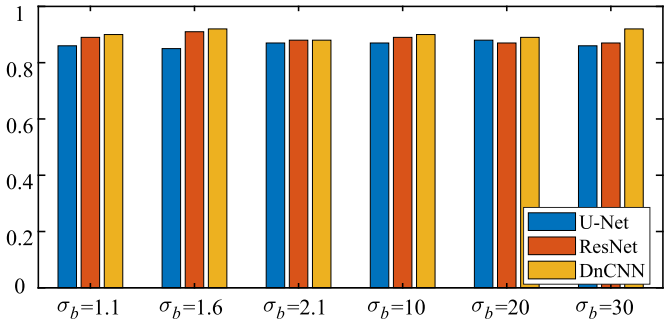


Fig. 6. KS of kernels refined by different networks: U-Net, ResNet, and DnCNN. These networks are all set to 17 layers and their performance on kernel refinement are very close. The DnCNN takes slight advantage over other networks in our implementation.

E. Stage Three: Low-Rank Decomposition Nonblind Deblur

Once the blur kernel has been estimated, the blind deblurring task has been converted to an easier nonblind deblurring task. However, the stripe noise still causes an adverse effect and would be unexpectedly amplified. Thus, the conventional nonblind deblurring [75] cannot be simply applied. In this work, we consider stripe noise via (4) and remove the stripe noise during the nonblind deblurring procedure. We have analyzed in Section III-A that deblurring and destriping should be coupled. To achieve this, we start from the image decomposition perspective to iteratively estimate the clean image and stripe component. Rewriting (1) in the form of matrix and vector, we have

$$\min_{\boldsymbol{O},\boldsymbol{E}} \frac{1}{2}\|\boldsymbol{G}-\boldsymbol{H}\boldsymbol{O}-\boldsymbol{E}\|_2^2+\tau P_o(\boldsymbol{O})+\mu P_e(\boldsymbol{E}) \tag{19}$$

where the first term is the data fidelity term to guarantee the restoration results to be consistent with the observation model and the second and third terms are the priors to regularize the clean image and stripe noise, respectively. Compared with the previous outlier deblurring methods, (19) could well remove the stripe, not simply discard them. Moreover, we do not explicitly detect the stripe noises, and even the images are completely covered by the stripes.

Thus, the core problem is how to choose the proper priors for the clean image and stripes. In Section III-C, we have shown that the stripe noise has distinct low-rank properties. Thus, we can obtain $P_e(\boldsymbol{E})=\|\boldsymbol{E}\|_*$, where the nuclear norm is the convex surrogate functional for the rank. As for the image, we would like to recover both the sharp edges and the fine texture. On one hand, TV regularization has been widely used due to its desirable properties such as convexity and the ability to preserve sharp edges [9]. On the other hand, the framelet [76], [77] could sparsely represent the multiscale image structures with multiresolution analysis in the framelet transformation domain. In this work, we show that TV and framelet could benefit each other for image representation. Thus, we propose the low-rank decomposition-based joint deblurring and destriping model as follows:

$$\min_{\boldsymbol{O},\boldsymbol{E}} \frac{1}{2}\|\boldsymbol{H}\boldsymbol{O}+\boldsymbol{E}-\boldsymbol{G}\|_2^2+\tau_1\|\nabla\boldsymbol{O}\|_1+\tau_2\|\boldsymbol{W}\boldsymbol{O}\|_1+\mu\|\boldsymbol{E}\|_* \tag{20}$$

where μ, τ_1, and τ_2 are regularization parameters and $\boldsymbol{W}$ is the templates of framelet decomposition, and the implementation details can refer to [77]. Note that, the framelet is not learned but with the fixed template. $\tau_1=[\tau_{1x},\tau_{1y}]$ includes both the horizontal and vertical constraints for simplicity. In (20), both deblurring and destriping are iteratively performed: a better destriping result would ease the deblurring and a better deblurring result would promote destriping in turn. We still adopt the alternating minimization scheme to solve (20) with respect to the clean image $\boldsymbol{O}$ and stripe noise $\boldsymbol{E}$.

1) Stripe Noise $\boldsymbol{E}$ Estimation: With the image $\boldsymbol{O}$ fixed, (20) can be relaxed as

$$\boldsymbol{E}=\arg\min_{\boldsymbol{E}} \frac{1}{2}\|\boldsymbol{H}\boldsymbol{O}+\boldsymbol{E}-\boldsymbol{G}\|_2^2+\mu\|\boldsymbol{E}\|_*. \tag{21}$$

Equation (21) is a classical low-rank matrix recovery problem with closed-form solution, which can be easily solved by a soft-thresholding operation on the singular values of observation matrix [78]

$$\begin{cases}\boldsymbol{E}=\boldsymbol{U}\big(\text{shrink}_{L_*}(\Sigma,\mu)\big)\boldsymbol{V}^{\boldsymbol{T}}\\ \text{shrink}_{L*}(\Sigma,\mu)=\text{diag}\{\max(\Sigma_{ii}-\mu,0)\}_i\end{cases} \tag{22}$$

where Σ_{ii} is the diagonal element of the singular value decomposition (SVD) $\boldsymbol{H}\boldsymbol{O}-\boldsymbol{G}=\boldsymbol{U}\Sigma\boldsymbol{V}^T$.

2) Clean Image $\boldsymbol{O}$ Estimation: With the stripe $\boldsymbol{E}$ fixed, (20) can be relaxed as

$$\boldsymbol{O}=\arg\min_{\boldsymbol{O}} \frac{1}{2}\|\boldsymbol{H}\boldsymbol{O}+\boldsymbol{E}-\boldsymbol{G}\|_2^2+\tau_1\|\nabla\boldsymbol{O}\|_1+\tau_2\|\boldsymbol{W}\boldsymbol{O}\|_1. \tag{23}$$

Considering that the l_1-norm is nondifferentiable, we introduce the splitting Bregman iteration [70] with two auxiliary variables $\boldsymbol{M_1}=\nabla\boldsymbol{O}$, $\boldsymbol{M_2}=\boldsymbol{W}\boldsymbol{O}$

$$\begin{aligned}\{\boldsymbol{O},\boldsymbol{M_1},\boldsymbol{M_2}\}=\arg\min_{\boldsymbol{O},\boldsymbol{M_1},\boldsymbol{M_2}} &\frac{1}{2}\|\boldsymbol{H}\boldsymbol{O}+\boldsymbol{E}-\boldsymbol{G}\|_2^2+\tau_1\|\boldsymbol{M}_1\|_1\\ &+\tau_2\|\boldsymbol{M}_2\|_1+\frac{\alpha_1}{2}\|\boldsymbol{M}_1-\nabla\boldsymbol{O}-\boldsymbol{Q}_1\|_2^2\\ &+\frac{\alpha_2}{2}\|\boldsymbol{M}_2-\boldsymbol{W}\boldsymbol{O}-\boldsymbol{Q}_2\|_2^2.\end{aligned} \tag{24}$$

Furthermore, the functional (24) is converted into two separate easier subproblems

$$\begin{aligned}\boldsymbol{O}=\arg\min_{\boldsymbol{O}} &\frac{1}{2}\|\boldsymbol{H}\boldsymbol{O}+\boldsymbol{E}-\boldsymbol{G}\|_2^2+\frac{\alpha_1}{2}\|\boldsymbol{M}_1-\nabla\boldsymbol{O}-\boldsymbol{Q}_1\|_2^2\\ &+\frac{\alpha_2}{2}\|\boldsymbol{M}_2-\boldsymbol{W}\boldsymbol{O}-\boldsymbol{Q}_2\|_2^2\end{aligned} \tag{25}$$

$$\begin{cases}\boldsymbol{M}_1=\arg\min_{\boldsymbol{M_1}}\alpha_1\|\boldsymbol{M}_1-\nabla\boldsymbol{O}-\boldsymbol{Q}_1\|_2^2+\tau_1\|\boldsymbol{M}_1\|_1\\ \boldsymbol{M}_2=\arg\min_{\boldsymbol{M_2}}\alpha_2\|\boldsymbol{M}_2-\boldsymbol{W}\boldsymbol{O}-\boldsymbol{Q}_2\|_2^2+\tau_2\|\boldsymbol{M}_2\|_1.\end{cases} \tag{26}$$

Note that, $\boldsymbol{W}^T\boldsymbol{W}=\boldsymbol{I}$, and thus, (25) can be computed by FFT [see (27)], as shown at the bottom of the next page.

The auxiliary variables $\boldsymbol{M}_1$ and $\boldsymbol{M}_2$ are solved by the soft-threshold shrinkage formulation [70]

$$\begin{cases}\boldsymbol{M}_1=\max\{\big|\nabla\boldsymbol{O}+\boldsymbol{Q}_1\big|-\dfrac{\tau_1}{\alpha_1},0\}\cdot\text{sign}(\nabla\boldsymbol{O}+\boldsymbol{Q}_1)\\ \boldsymbol{M}_2=\max\{\big|\boldsymbol{W}\boldsymbol{O}+\boldsymbol{Q}_2\big|-\dfrac{\tau_2}{\alpha_2},0\}\cdot\text{sign}(\boldsymbol{W}\boldsymbol{O}+\boldsymbol{Q}_2)\end{cases} \tag{28}$$

Authorized licensed use limited to: XIDIAN UNIVERSITY. Downloaded on November 24,2022 at 09:16:45 UTC from IEEE Xplore. Restrictions apply.

Algorithm 2 Low-Rank Decomposition Nonblind Deblur

Require: Degraded image $\boldsymbol{G}$, Blur kernel $\boldsymbol{H}$.
1: **Initialize:** μ, τ_1, τ_2; $\boldsymbol{Q}_1^1 = \boldsymbol{Q}_2^1 = 0$; K_{max}, T_{max};
2: **for** $k = 1$ to K_{max} **do**
3: **Stripe Estimation**: Solve $\boldsymbol{E}^{k+1}$ by (22);
4: **for** $t = 1$ to T_{max} **do**
5: **Clean Image**: Solve $\boldsymbol{O}^{t+1}$ by (27);
6: **Auxiliary Variables**: Solve $\boldsymbol{M}_1^{t+1}$, $\boldsymbol{M}_2^{t+1}$ by (28);
7: **Bregman Iteration**: Update $\boldsymbol{Q}_1^{t+1}$, $\boldsymbol{Q}_2^{t+1}$ by (29);
8: **end for**
9: **end for**
Ensure: Clean image $\boldsymbol{O}$ and stripe noise $\boldsymbol{E}$.

where sign is the sign function in which the positive number equals 1 and the negative number equals 0. The Bregman variables $\boldsymbol{Q}_1$ and $\boldsymbol{Q}_2$ are updated by

$$\begin{cases} \boldsymbol{Q}_1^{t+1} = \boldsymbol{Q}_1^t + \nabla \boldsymbol{O} - \boldsymbol{M}_1 \\ \boldsymbol{Q}_2^{t+1} = \boldsymbol{Q}_2^t + \boldsymbol{W}\boldsymbol{O} - \boldsymbol{M}_2. \end{cases} \tag{29}$$

We summarize the jointly nonblind deblurring and destriping process as in Algorithm 2.

V. Experimentation

A. Experimental Setting

We evaluate the competing methods on different remote sensing datasets, including GeoEye and HSI. Specifically, we collect 100 256×256 GeoEye images and 100 256×256 HSI images for testing. Moreover, to verify the robustness of the proposed RBDS method, we test the competing methods on real striped and blurry images with different imaging systems: HSI, thermal images, and CCD images. The source code and datasets would be released at the homepage of the authors.[3]

We compare the RBDS with state-of-the-art blind deblurring under striping. We choose two optimization-based methods: outlier-based blind deblurring method (BDO) [25] and joint blind deblurring and destriping (JBDD) method [27] for comparison. Moreover, we combine the competitive destriping method SGE [35] and the blind deblurring method RGTV [65]. The GAN-based methods (CycleGAN [79] and DeblurGAN [49]) and the CNN-based methods (SRD [21] and MPRNet [80]) are also selected for comparison. They are retrained on our training dataset for a fair comparison. Note that, the proposed method is very robust for parameter setting. We empirically fix the parameters as follows: $\lambda = 5$, $\gamma = 5$, learning rate 10^{-4}, batch size 4096, $\mu = 5\text{e}^{-3}$, $\tau_1 = [1\text{e}^{-2}, 2.5\text{e}^{-3}]$, and $\tau_2 = 0.06$.

[3]https://owuchangyuo.github.io/

B. Restoration Results on Simulated Datasets

In this section, we conduct qualitative and quantitative experiments to compare different methods on different datasets. We show the restoration results on the simulation dataset with the different stripe noise levels and blur levels in Fig. 7. The outlier-based deblurring method (BDO) cannot handle the overwhelming stripe noise. Although the blur effect can be recovered to some extent, the stripe noise has been unexpectedly amplified due to the deconvolution process. Besides, the results of combined RGTV + SGE in Fig. 7(e) show that the post-destriping is far to effectively suppress the amplified stripe noise. On the contrary, the compositional SGE + RGTV can well remove the stripe noise but at the cost of losing high-frequency details. For the learning-based method, CycleGAN and DeblurGAN tend to produce artifacts that are common for the GAN-based method, and it can be seen in the close-up of Fig. 7(f) and (g). Besides, they are not robust to different images and degradation levels. The JBDD could achieve well competitive results, and however, the image details, especially the vertical image structure, have been damaged. The JBDD does not explicitly model the stripe noise, so it may have to remove the vertical structures redundantly. As a result, the image structures similar to stripe noise are unwillingly smoothed out. The proposed RBDS method achieves the best performance in terms of stripe noise suppression and high-frequency detail recovery.

In Table I, we present the quantitative index on different datasets with different degradation levels. The image quality assessment PSNR and SSIM [81] are employed for quantitative assessment. The BDO even obtains inferior results than that of the input degraded images, which means that the outlier-based deblurring methods cannot be easily applied to our task. The learning-based methods DeblurGAN and CycleGAN can slightly improve the image quality. Compared with other methods, the proposed method consistently achieves the best values under all cases, which further demonstrates the superiority of the proposed RBDS method in terms of performance and generalization.

C. Restoration Results on Real Degradation

We further validate the proposed RBDS method on real degradation on remote sensing images, and the restoration results are shown in Fig. 8. From the top to the bottom, we test the real HSI, thermal image, and also the CCD image. Note that, although the causes of the stripe artifacts are different in various imaging systems, Fig. 8(a) shows vertical line-pattern structures. We can observe that the proposed method Fig. 8(h) consistently recovers the image details and meanwhile well removes the stripe noises. Moreover, the restored image of the proposed method contains much sharper edges with less stripe residual. The combination method SGE + RGTV performs destriping and deblurring successively and the results are

$$\boldsymbol{O} = \mathcal{F}^{-1}\left(\frac{\overline{\mathcal{F}}(\boldsymbol{H}) \cdot \mathcal{F}(\boldsymbol{G} - \boldsymbol{E}) + \alpha_1 \overline{\mathcal{F}}(\nabla) \cdot \mathcal{F}(\boldsymbol{M}_1 - \boldsymbol{Q}_1) + \alpha_2 \mathcal{F}(\boldsymbol{W}^T(\boldsymbol{M}_2 - \boldsymbol{Q}_2))}{\alpha_1 \overline{\mathcal{F}}(\nabla) \cdot \mathcal{F}(\nabla) + \overline{\mathcal{F}}(\boldsymbol{H}) \cdot \mathcal{F}(\boldsymbol{H}) + \alpha_2 \boldsymbol{I}}\right) \tag{27}$$

Authorized licensed use limited to: XIDIAN UNIVERSITY. Downloaded on November 24,2022 at 09:16:45 UTC from IEEE Xplore. Restrictions apply.

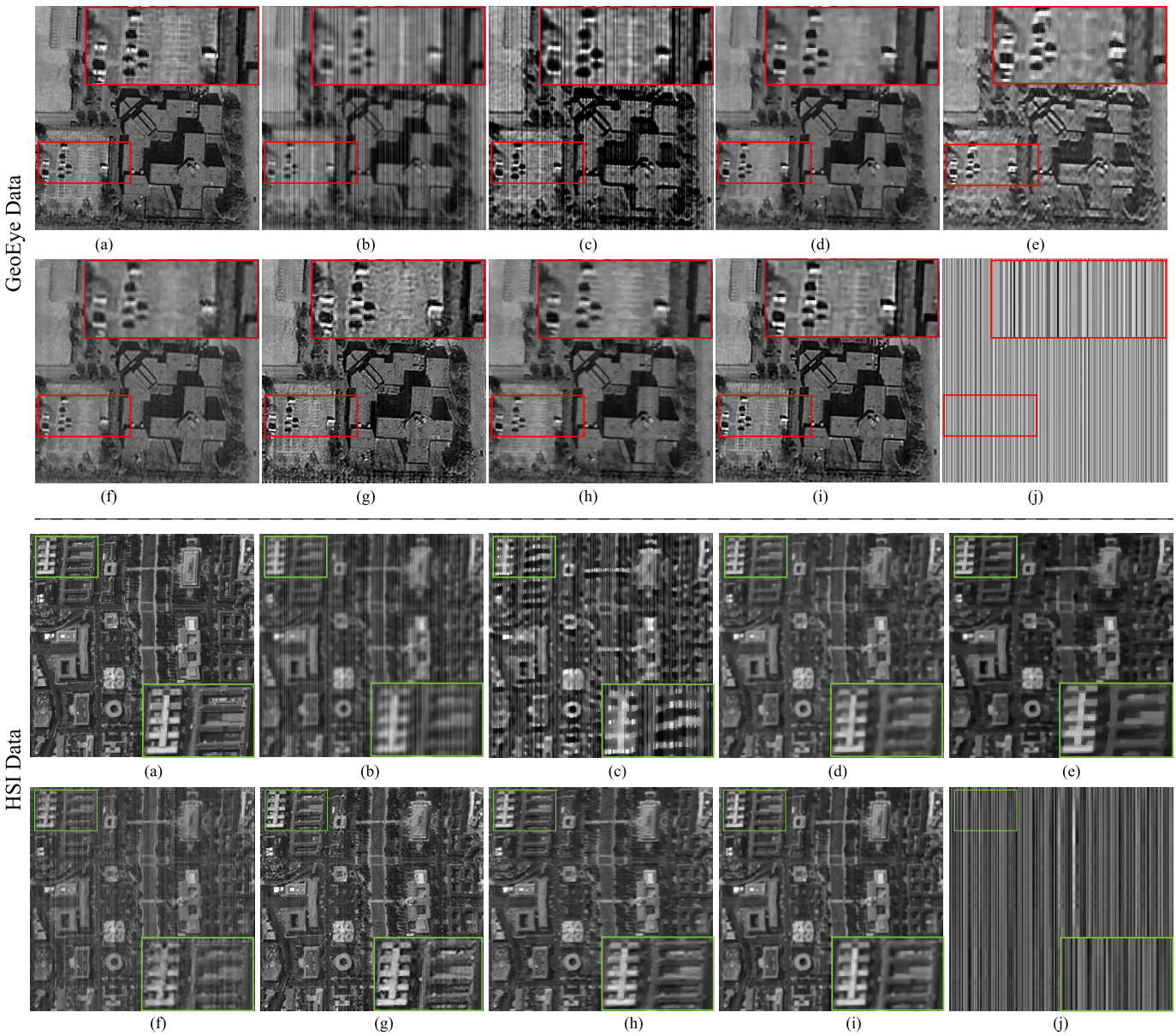


Fig. 7. Qualitative evaluation on GeoEye (stripe noise level $\sigma_e = 30$ and blur level $\sigma_b = 1.1$) and HSI dataset (stripe noise level $\sigma_e = 10$ and blur level $\sigma_b = 1.6$). (a) Clean image. (b) Degraded image. (c) BDO. (d) SGE + RGTV. (e) RGTV+SGE. (f) CycleGAN. (g) DeblurGAN. (h) JBDD. (i) RBDS. (j) Estimated stripe.

shown in Fig 8(b). This method either smoothed the image details for completely removing stripe noise or amplifies the residual stripe noise due to deconvolution because it is hard for the combination methods to resolve the contradictions between destriping and deblurring, as analyzed in Section III-A. The JBDD considers this contradiction and iteratively performs destriping and deblurring in a unified framework. However, the JBDD tends to suppress the vertical image structures that are similar to stripe noise, as shown in Fig. 8(c), since it does not explicitly model the stripe noise to extract the clean image from stripe noise. For the learning-based methods, they lack the generalization ability to real scenes. The detailed analysis will be given in Section V-D. The proposed RBDS method reaches the best effectiveness and generalization ability against the compared methods.

D. Discussion

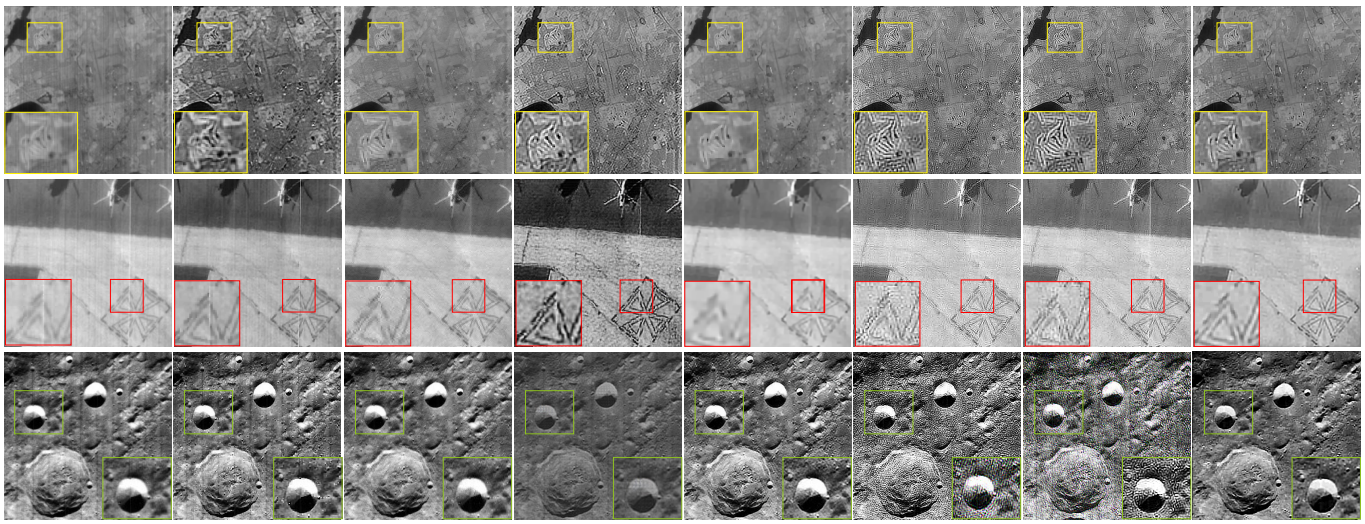
1) Robustness to Different Images Modalities and Degradation Levels: In practice, the image modalities and stripe/blur levels are usually different, and the influence of degradations varies across different bands. First, we demonstrate that the proposed RBDS method is very robust to different imaging systems in Figs. 7–9. We test the algorithms on three types of modalities: infrared image, PMMW image, and scanning electron microscope (SEM) images, whose causes of stripe noise are different. The RBDS can effectively remove stripe noise and recover the sharp clean image, as shown in Fig. 9(i). Second, we show the restoration results under different degradation levels in Fig. 10(a) and (b). We can observe that the proposed method consistently achieves the best restoration results. Note that, the performance of the

Authorized licensed use limited to: XIDIAN UNIVERSITY. Downloaded on November 24,2022 at 09:16:45 UTC from IEEE Xplore. Restrictions apply.

TABLE I

RESTORATION RESULTS UNDER VARIOUS BLUR AND NOISE LEVELS ON THE GEOEYE AND HSI DATASETS. THE BEST IS HIGHLIGHTED IN BOLD

Dataset	Blur	Stripe	Methods						
			Degraded	BDO [25]	SGE [35] + RGTV [65]	CycleGAN [79]	DeblurGAN [49]	JBDD [27]	RBDS
GeoEye	σ_b = 1.1	σ_e = 10	23.53/0.6893	19.86/0.5588	25.83/0.8181	25.19/0.8237	24.44/0.7697	25.84/0.8127	**27.07/0.8557**
		σ_e = 20	22.10/0.5669	17.61/0.4649	25.73/0.8165	24.86/0.7992	24.36/0.7672	25.26/0.8018	**26.69/0.8468**
		σ_e = 30	20.52/0.4590	15.74/0.3373	25.05/0.8066	24.42/0.7890	23.86/0.7593	24.76/0.7983	**25.61/0.8317**
	σ_b = 1.6	σ_e = 10	21.54/0.5486	19.08/0.5137	23.19/0.6918	24.63/0.7910	24.07/0.7655	23.02/0.6798	**26.27/0.8420**
		σ_e = 20	20.67/0.4471	17.02/0.4139	23.08/0.6847	24.29/0.7882	23.74/0.7433	22.66/0.6826	**24.87/0.7996**
		σ_e = 30	19.35/0.3559	15.47/0.3001	22.73/0.6812	23.61/0.7379	23.56/0.7350	22.45/0.6727	**24.40/0.7917**
	σ_b = 2.1	σ_e = 10	20.51/0.4634	19.60/0.3906	21.61/0.5900	21.80/0.5978	21.71/0.5958	21.34/0.5644	**22.69/0.6847**
		σ_e = 20	19.76/0.3631	16.72/0.2739	21.36/0.5827	21.61/0.5837	21.52/0.5846	21.13/0.5631	**22.21/0.6659**
		σ_e = 30	18.82/0.2933	15.43/0.2343	21.24/0.5783	21.31/0.5505	21.19/0.5650	21.07/0.5624	**21.88/0.6176**
HSI	σ_b = 1.1	σ_e = 10	23.97/0.7475	20.10/0.5612	26.07/0.8233	24.79/0.7915	24.02/0.7359	25.83/0.8267	**27.21/0.8957**
		σ_e = 20	22.58/0.6999	17.97/0.4689	25.95/0.8191	22.48/0.7192	23.12/0.6961	25.46/0.8126	**26.89/0.8868**
		σ_e = 30	21.10/0.6622	15.94/0.3389	25.15/0.8164	20.68/0.6931	22.16/0.6435	24.96/0.8003	**25.85/0.8517**
	σ_b = 1.6	σ_e = 10	21.84/0.6370	19.48/0.5183	23.53/0.7106	22.23/0.6091	22.33/0.5797	23.12/0.6912	**26.49/0.8341**
		σ_e = 20	20.99/0.5949	17.10/0.4147	23.24/0.7005	21.95/0.5711	22.02/0.5659	22.82/0.6642	**25.09/0.7716**
		σ_e = 30	19.77/0.4095	15.85/0.3021	22.97/0.6842	21.29/0.5651	20.92/0.5124	22.67/0.6573	**24.61/0.7517**
	σ_b = 2.1	σ_e = 10	20.47/0.5292	19.84/0.3936	21.73/0.5988	21.16/0.5652	21.01/0.5068	21.48/0.5872	**22.79/0.6547**
		σ_e = 20	19.84/0.4455	16.74/0.2739	21.50/0.5835	20.77/0.5327	20.86/0.4962	21.31/0.5801	**22.41/0.6059**
		σ_e = 30	19.02/0.3119	15.63/0.2363	21.38/0.5865	20.19/0.5293	20.39/0.4748	21.21/0.5676	**22.11/0.6175**



(a) (b) (c) (d) (e) (f) (g) (h)

Fig. 8. Real restoration results for different kinds of remote sensing images with different causes of stripe and blur. (a) Degraded image, restored results by (b) SGE + RGTV, (c) JBDD, (d) CycleGAN, (e) DeblurGAN, (f)SRNet, (g) MPRNet, and (h) RBDS.

learning-based CycleGAN and DeblurGAN varies a lot for different cases. On the contrary, our method inherits both the good generalization of the optimization model and the powerful representation of CNN.

2) Comparison With Learning-Based Methods: We further discuss the advantages of the proposed RBDS method over the learning-based methods. For the GAN-based methods, the DeblurGAN can somewhat recover the clean image but suffer from oversmooth of the image structures or the artifacts, as shown in Figs. 8(d) and 9(d). The CycleGAN would also generate artifacts and even appear intensity bias, as shown in Figs. 8(d) and 9(e). It is difficult for the GAN-based method to adapt complex scenes and degradations. The CNN-based methods of SRD and MPRNet can also recover the image to some extent, and they would introduce unexpected ringing artifacts or residual stripe noise, as shown in Figs. 8(g) and (h) and 9(g) and (h). The main reason is the domain gap between the synthetic training and real testing datasets, which makes the learning-based CNN methods less generalized well for real cases. On the contrary, the RBDS integrates the generalization of physical model-driven optimization and good representation of data-driven learning networks. The real experiments support the advantage of RBDS over the learning-based CNN methods in terms of generalization.

3) Effectiveness of the Blur Kernel Refinement: To verify the accuracy of the estimated kernel, we also show the kernel similarity (KS) [14] between the estimated kernel and the ground-truth kernel under different cases. In Fig. 10(c) and (d), we have the following observations. First, comparing the red curve (stage2) and green curve (stage1), the kernel refinement

Authorized licensed use limited to: XIDIAN UNIVERSITY. Downloaded on November 24,2022 at 09:16:45 UTC from IEEE Xplore. Restrictions apply.

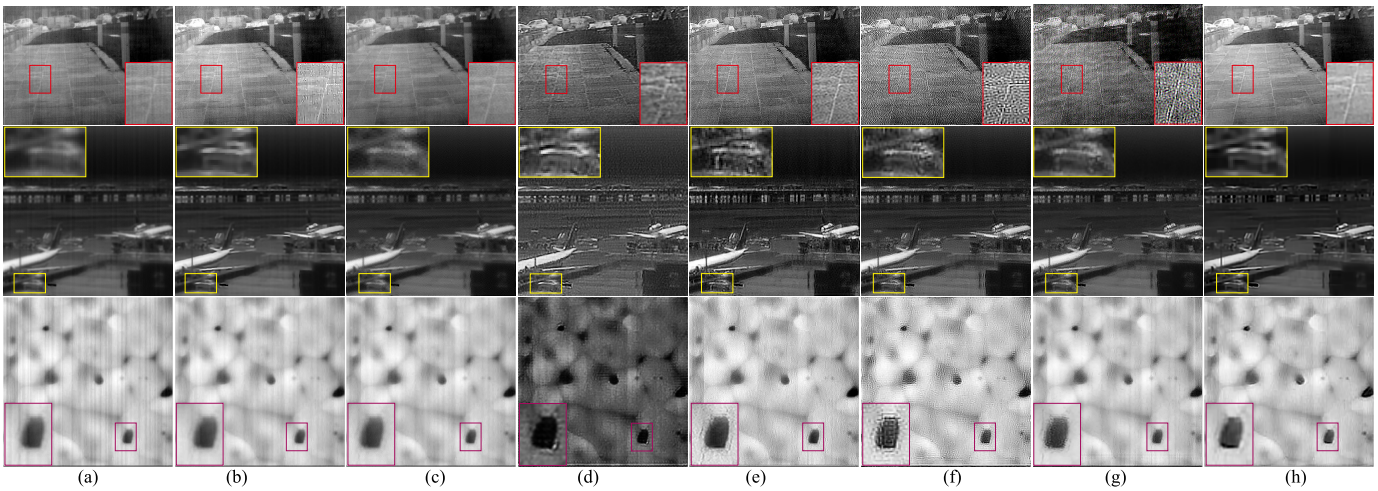


Fig. 9. Real restoration results for striped and blurry images of different modalities. (From Top to Bottom) Infrared images, PMMW images, and SEM images. (a) Degraded image, restored results by (b) SGE + RGTV, (c) JBDD, (d) CycleGAN, (e) DeblurGAN, (f)SRNet, (g) MPRNet, and (h) RBDS.

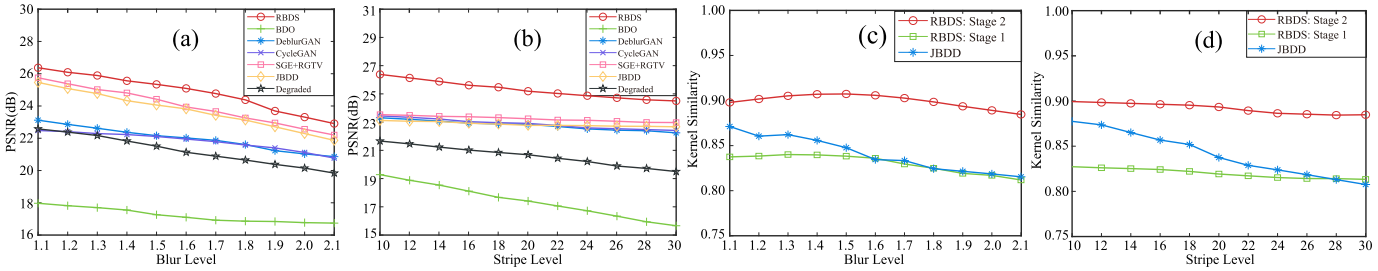


Fig. 10. Quantitative evaluation of robustness to different degradation levels. The blur level means the variance of Gaussian blur kernel and the stripe level means the intensity range. We show both the restoration results of the clean image and blur kernel. (a) and (b) Image similarity between the estimated image and the ground-truth image. (c) and (d) KS between the estimated kernel and ground-truth kernel.

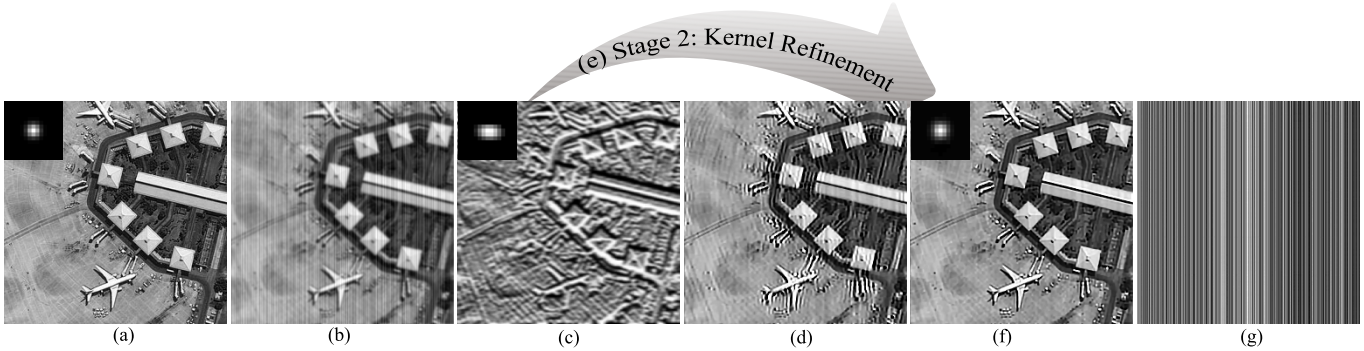


Fig. 11. Visualization of each step. (a) Ground truth. (b) Degraded image. (c) Estimated kernel and corresponding saliency edges by stage1. (d) Estimated inaccurate image via intermediated blur kernel in stage1. (e) Kernel refinement by stage2. (f) Estimated final image by stage3. (g) Estimated stripe by stage3.

in stage 2 is indeed useful. Second, the proposed method is very robust to the different degradation levels in terms of noise and blur. The blur curve (JBDD) decreases rapidly with the increase of the degradation levels, while the RBDS method almost does not change at all. Third, the RBDS method could obtain a much more accurate kernel, compared with the JBDD.

We visualize both the kernel and image in each step in Fig. 11. The unidirectional kernel estimation in stage 1 could partially provide the blur kernel cues. In Fig. 11(d), we directly feed the kernel estimated in stage 1 to recover the clean image. We can observe that there exist obvious ringing artifacts. After the kernel refinement in Fig. 11(e), the KS significantly improves from 0.8914 to 0.9875. Then, the nonblind joint image deblurring and destriping results are performed, and the estimated clean image and stripes are shown in Fig. 11(f) and (g), respectively. The image and stripes are satisfactorily decoupled. Moreover, the estimated image contains very sharp edges with very clear targets.

4) Robustness to the Spectral Variability: We further analyze the performance of the proposed method when meeting spectral variability [82]. We test the proposed RBDS method across different bands of the PaviaU image. Every band is

Authorized licensed use limited to: XIDIAN UNIVERSITY. Downloaded on November 24,2022 at 09:16:45 UTC from IEEE Xplore. Restrictions apply.

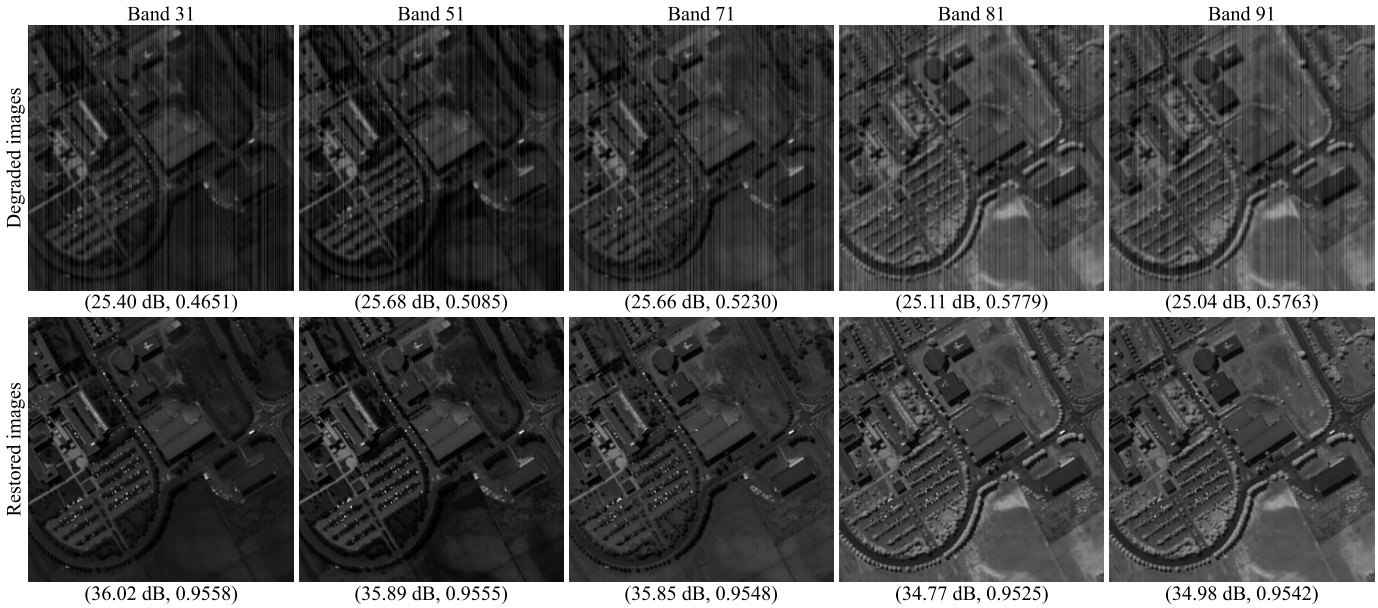


Fig. 12. Analysis of robustness of the proposed RBDS method on spectral variability. The first row is degraded images and the second row is restored images at bands 31, 51, 71, 81, and 91.

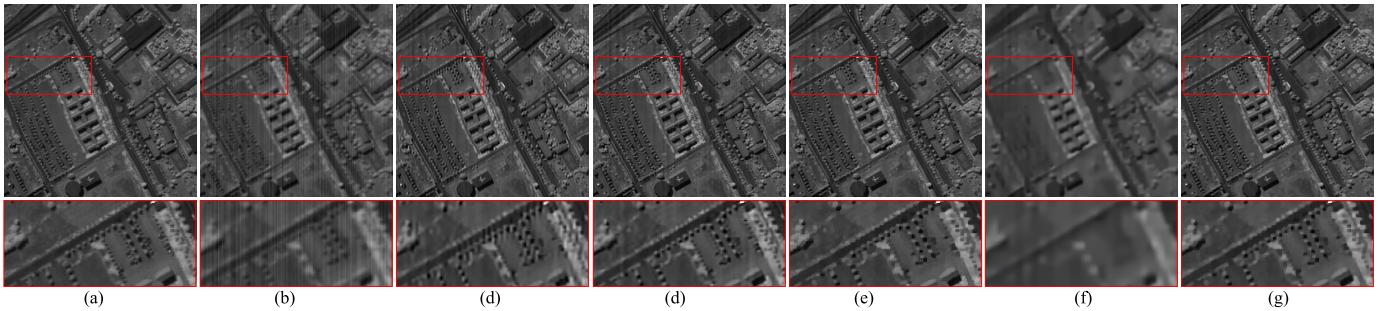


Fig. 13. Effectiveness of stage 2: kernel refinement and each term in stage 3: low-rank decomposition-based nonblind deblurring and destriping. (a) Original (PSNR, SSIM). (b) Degraded (28.27, 0.7417). (c) w/o kernel refinement (28.76, 0.8279). (d) w/o TV (31.14, 0.9080). (e) w/o framelet (32.33, 0.9235). (f) w/o low rank (25.84, 0.6063). (g) RBDS (32.83, 0.9318).

imposed with the same blur and stripe level, but the influences are different due to spectral variability. We can observe in Fig. 12 that the proposed RBDS can consistently improve the image quality qualitatively and quantitatively for each band. The restored results suggest that the RBDS is very robust when meeting spectral variability.

5) Ablation Study: The ablation analysis of stage-2 and the priors in stage-3 has been reported in Table II. Also, we provide one visual example for better understanding. We have three key observations in Fig. 13. First, after employing the stage-2 kernel refinement, the performance significantly improves, which greatly validates the effectiveness of the kernel refinement. Second, without the TV term for the image, the performance drops rapidly since the TV is used to distinguish the sharp image edges from the stripe noise. Moreover, without the framelet term for the image, the performance drops slightly since the framelet is used to represent the singular image textures, namely, the image details for restoration. We can conclude that the TV and framelet collaboratively model both the large- and small-scale image features. Third, without the low-rank prior for the stripe, the proposed method fails to achieve satisfactory results, which indicates the importance of low-rank decomposition model.

TABLE II

ABLATION STUDY ON DIFFERENT TERMS OF KERNEL REFINEMENT, TV PRIOR, FRAMELET PRIOR, AND LOW-RANK PRIOR

Stage-2	Stage-3			Index	
Kernel-Refinement	TV	Framelet	Low-Rank	PSNR ↑	SSIM ↑
✓	✓	✓	✓	**24.03**	**0.7259**
✓	✗	✓	✓	22.67	0.6813
✓	✓	✗	✓	23.22	0.7009
✓	✓	✓	✗	20.48	0.4806
✗	✓	✓	✓	**21.79**	**0.6534**
✗	✗	✓	✓	21.05	0.6153
✗	✓	✗	✓	21.54	0.6184
✗	✓	✓	✗	18.61	0.4367

6) Robust to the Training Dataset: We would like to emphasize that the proposed method is not to learn the image but instead to learn the blur kernel, that is to say, the network mainly pays attention to the blur kernel, not the image. This is

Authorized licensed use limited to: XIDIAN UNIVERSITY. Downloaded on November 24,2022 at 09:16:45 UTC from IEEE Xplore. Restrictions apply.

TABLE III
RUNNING TIME OF EACH METHOD (SECONDS)

Method	BDO [25]	SGE [35] + RGTV [65]	CycleGAN [79](GPU/CPU)	DeblurGAN [49]	JBDD [27]	RBDS
Time	77.49	9.58	0.23/1.98	0.25/2.73	1.52	12.32

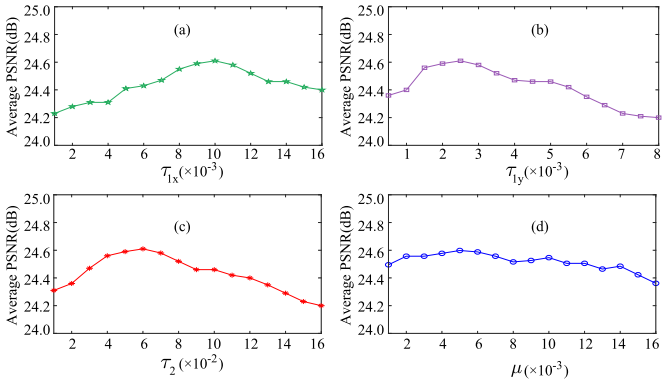


Fig. 14. Influence of the parameters $\tau_1 = [\tau_{1x}, \tau_{1y}]$, τ_2, and μ in the low-rank decomposition nonblind deblur model. (a)–(d) PSNR values of restoration results with different regularization parameters of τ_{1x}, τ_{1y}, τ_2, and μ, respectively.

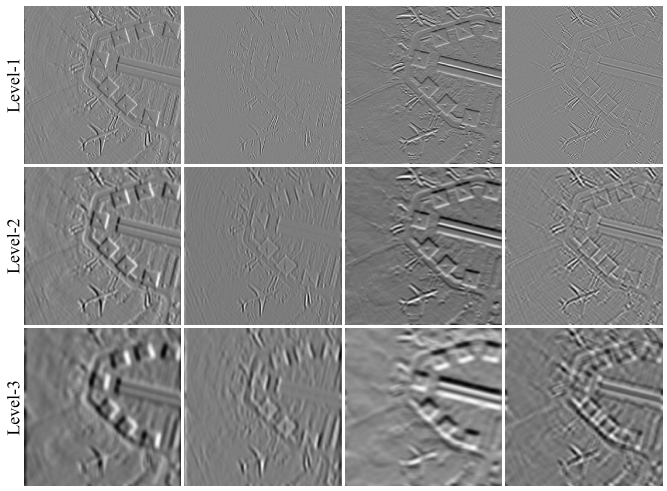


Fig. 15. Visualization of the framelet coefficient maps of a remote sensing image at different levels. (From Top to Bottom rows) Coefficient maps at different levels, which suggest the image representation at different scales (three levels in our implementation). (From Left to Right) Coefficient maps under different framelet templates. The coefficient maps all consistently sparse-response discriminative features for image representation.

the major difference between the proposed method and classical learning-based methods. Moreover, our RBDS is a jointly physical model-driven optimization and data-driven learning network method, which means that the proposed method could reduce the dependence on training data. Thus, our method can be trained and tested on arbitrary image modalities, which have been validated by real data experiments. Besides, the key to the single image deblurring for the blur kernel estimation is the large-scale salient edges [12]. Both the natural images and remote sensing images could contain the large-scale salient edges, indicating that it might be no significant bias between them on kernel estimation. The Place2 dataset has diverse scenes and sufficient amounts of samples that are beneficial to training the blur kernel.

7) Robustness to Parameters: The regularization parameters, τ_1 of the TV term, τ_2 of the framelet term, and μ of the low-rank term, have important influences on restoration results. They are evaluated on our simulation datasets: one is varying, while the others are fixed to the optimal setting. Fig. 14 shows the average PSNR value of restoration results varying with the parameter. Although the range of parameters is relatively large, the PSNR value remains relatively stable (the variation range is less than 0.5 dB). It validates that our method is robust to parameter setting.

8) Effectiveness of Framelet Representation: The frame coefficient $\boldsymbol{WO}$ is constrained by the l_1-norm-based sparse prior $\|\boldsymbol{WO}\|_1$ in our implementation. The framelet decomposition has the ability of multiscale representation by utilizing multilevel decomposition. In Fig. 15, we provide an intuitive visualization of the framelet decomposition of a remote sensing image. We can observe that the framelet could well extract different scale coarse-to-fine image features (bottom-up rows) and also different interest features (left-to-right columns). Moreover, the coefficient maps all consistently sparse-response discriminative features for image representation. Thus, the spare prior $\|\boldsymbol{WO}\|_1$ is utilized in our nonblind deblurring framework for clean image representation.

9) Running Time Analysis: The time consumption of different methods is compared in Table III. We report the running time of the competing methods on the image with size 256×256. All codes are executed on MATLAB R2019a, an Intel i9 CPU at 3.60 GHz, 32-GB memory, and NVIDIA 2080Ti GPU. We can observe that the learning-based methods CycleGAN and DeblurGAN infer fast even on the CPU platform. The optimization-based JBDD achieves good performance in terms of running time since it is one-stage framework. The outlier-based method BDO is the slowest of the competing methods since it involves a lot of iterations for converging. The computational complexity of the proposed RBDS method is relatively high. Next, we provide a detailed time consumption analysis of each stage and subproblem.

The total running time of the three stages of the proposed method is 12.32 s, which takes 1.82, 0.09, and 10.41 s, as shown in Table IV, that is to say, the blur kernel estimation and refinement in the first and second stage is not time-consuming. Thus, we further report the elapsed time of each subproblem in stage3, which includes the stripe noise $\boldsymbol{E}$ estimation and clean image $\boldsymbol{O}$ estimation, while the $\boldsymbol{O}$ estimation is further divided into four subproblems $\boldsymbol{U}$, $\boldsymbol{M}_1$, $\boldsymbol{M}_2$, and $\boldsymbol{Q}$. Note that the subproblem $\boldsymbol{E}$ estimation is computed once in every iteration, while the subproblems are computed three times in every iteration. We can observe that the $\boldsymbol{E}$ estimation is the most time-consuming since it involves the SVD operator. Besides, the framelet decomposition-related $\boldsymbol{U}$ and $\boldsymbol{M}_2$ are

Authorized licensed use limited to: XIDIAN UNIVERSITY. Downloaded on November 24,2022 at 09:16:45 UTC from IEEE Xplore. Restrictions apply.

TABLE IV
AVERAGE RUNNING TIME OF EACH STAGE AND SUBPROBLEM IN STAGE3 (SECONDS)

Overall (12.32)	Stage1		Stage2		Stage3
	1.82		0.09		10.41
Stage3 (10.41)	**E**	**U**	$\mathbf{M}_1$	$\mathbf{M}_2$	**Q**
	6.38	1.79	0.02	1.86	0.36

also time-consuming. Therefore, we would like to consider accelerating the SVD operator and explore more efficient priors to alternate framelet decomposition in future work.

VI. CONCLUSION

In this work, we target the new and practical problem: RBDS. We first propose a new degradation model to accommodate the stripe noise. Then, we analyze the influence of the stripe noise on blind image deblurring and also the difficulty of this problem. We discover that the key is to utilize the directionality of the stripe, as so to get rid of the stripe in both the kernel estimation and nonblind deblurring procedure. Consequently, we propose a three-stage restoration framework for this task. The first and second stages combine the physical model-driven optimization and data-driven learning network to progressively refine the kernel. The third stage low-rank decomposition restoration model could alternatively perform destriping and nonblind deblurring. Extensive experimental results on both the real and synthetic datasets demonstrate the effectiveness and generalization of the proposed RBDs method, and our method consistently outperforms the state-of-the-art methods.

Although this work has made a good attempt, there is plenty of room for improvement. First, in this work, we mainly focus on the single image case, while in HSIs, there exist multiple bands with high spectral relationships. The proposed RBDS method obtains good performance on the restoration, yet the abundant spectral correlation is ignored. The spectral correlation between adjacent bands may provide good reference information, which could be utilized to improve the restoration performance. We think that the multiband image deblurring under stripe noise may be a promising and practical research direction. Second, as we have analyzed before, the SVD operators in nonblind deconvolution take a lot of computing time and it is necessary to accelerate the SVD operator to make the deblurring algorithm more practical.

REFERENCES

[1] B. Rasti, Y. Chang, E. Dalsasso, L. Denis, and P. Ghamisi, "Image restoration for remote sensing: Overview and toolbox," *IEEE Geosci. Remote Sens. Mag.*, vol. 10, no. 2, pp. 201–230, 2022.

[2] D. Hong *et al.*, "Interpretable hyperspectral artificial intelligence: When nonconvex modeling meets hyperspectral remote sensing," *IEEE Geosci. Remote Sens. Mag.*, vol. 9, no. 2, pp. 52–87, Jun. 2021.

[3] M. Wang *et al.*, "Tensor decompositions for hyperspectral data processing in remote sensing: A comprehensive review," 2022, *arXiv:2205.06407*.

[4] M. Wang, Q. Wang, and J. Chanussot, "Tensor low-rank constraint and l_0 total variation for hyperspectral image mixed noise removal," *IEEE J. Sel. Topics Signal Process.*, vol. 15, no. 3, pp. 718–733, Feb. 2021.

[5] M. Wang, Q. Wang, J. Chanussot, and D. Hong, "l_0-l_1 hybrid total variation regularization and its applications on hyperspectral image mixed noise removal and compressed sensing," *IEEE Trans. Geosci. Remote Sens.*, vol. 59, no. 9, pp. 7695–7710, Sep. 2021.

[6] H. Shen and L. Zhang, "A MAP-based algorithm for destriping and inpainting of remotely sensed images," *IEEE Trans. Geosci. Remote Sens.*, vol. 47, no. 5, pp. 1492–1502, May 2008.

[7] X. Kuang, X. Sui, Q. Chen, and G. Gu, "Single infrared image stripe noise removal using deep convolutional networks," *IEEE Photon. J.*, vol. 9, no. 4, pp. 1–13, Aug. 2017.

[8] Y. Chang, M. Chen, L. Yan, X.-L. Zhao, Y. Li, and S. Zhong, "Toward universal stripe removal via wavelet-based deep convolutional neural network," *IEEE Trans. Geosci. Remote Sens.*, vol. 58, no. 4, pp. 2880–2897, Apr. 2019.

[9] T. F. Chan and C.-K. Wong, "Total variation blind deconvolution," *IEEE Trans. Image Process.*, vol. 7, no. 3, pp. 370–375, Mar. 1998.

[10] R. Fergus, B. Singh, A. Hertzmann, S. T. Roweis, and W. T. Freeman, "Removing camera shake from a single photograph," *ACM Trans. Graph.*, vol. 25, no. 3, pp. 787–794, Jul. 2006.

[11] Q. Shan, J. Jia, and A. Agarwala, "High-quality motion deblurring from a single image," *ACM Trans. Graph.*, vol. 27, no. 3, pp. 1–10, 2008.

[12] A. Levin, Y. Weiss, F. Durand, and W. T. Freeman, "Understanding and evaluating blind deconvolution algorithms," in *Proc. IEEE Conf. Comput. Vis. Pattern Recognit.*, Jun. 2009, pp. 1964–1971.

[13] S. Cho and S. Lee, "Fast motion deblurring," in *Proc. ACM SIGGRAPH Asia Papers (SIGGRAPH Asia)*, 2009, pp. 1–8.

[14] L. Xu and J. Jia, "Two-phase kernel estimation for robust motion deblurring," in *Proc. Eur. Conf. Comp. Vis. (ECCV)*, 2010, pp. 157–170.

[15] D. Krishnan, T. Tay, and R. Fergus, "Blind deconvolution using a normalized sparsity measure," in *Proc. CVPR*, Jun. 2011, pp. 233–240.

[16] L. Xu, S. Zheng, and J. Jia, "Unnatural L0 sparse representation for natural image deblurring," in *Proc. IEEE Conf. Comput. Vis. Pattern Recognit.*, Jun. 2013, pp. 1107–1114.

[17] J. Pan, Z. Hu, Z. Su, and M.-H. Yang, "Deblurring text images via L0-regularized intensity and gradient prior," in *Proc. IEEE Conf. Comput. Vis. Pattern Recognit.*, Jun. 2014, pp. 2901–2908.

[18] C. J. Schuler, M. Hirsch, S. Harmeling, and B. Schölkopf, "Learning to deblur," *IEEE Trans. Pattern Anal. Mach. Intell.*, vol. 38, no. 7, pp. 1439–1451, Jul. 2015.

[19] A. Chakrabarti, "A neural approach to blind motion deblurring," in *Proc. Eur. Conf. Comp. Vis. (ECCV)*, 2016, pp. 221–235.

[20] J. Pan, D. Sun, H. Pfister, and M.-H. Yang, "Deblurring images via dark channel prior," *IEEE Trans. Pattern Anal. Mach. Intell.*, vol. 40, no. 10, pp. 2315–2328, Oct. 2017.

[21] X. Tao, H. Gao, X. Shen, J. Wang, and J. Jia, "Scale-recurrent network for deep image deblurring," in *Proc. IEEE/CVF Conf. Comput. Vis. Pattern Recognit.*, Jun. 2018, pp. 8174–8182.

[22] Y.-W. Tai and S. Lin, "Motion-aware noise filtering for deblurring of noisy and blurry images," in *Proc. IEEE Conf. Comput. Vis. Pattern Recognit.*, Jun. 2012, pp. 17–24.

[23] L. Zhong, S. Cho, D. Metaxas, S. Paris, and J. Wang, "Handling noise in single image deblurring using directional filters," in *Proc. IEEE Conf. Comput. Vis. Pattern Recognit.*, Jun. 2013, pp. 612–619.

[24] S. Cho, J. Wang, and S. Lee, "Handling outliers in non-blind image deconvolution," in *Proc. Int. Conf. Comput. Vis.*, Nov. 2011, pp. 495–502.

[25] J. Dong, J. Pan, Z. Su, and M.-H. Yang, "Blind image deblurring with outlier handling," in *Proc. IEEE Int. Conf. Comput. Vis. (ICCV)*, Oct. 2017, pp. 2478–2486.

[26] L. Chen, F. Fang, J. Zhang, J. Liu, and G. Zhang, "OID: Outlier identifying and discarding in blind image deblurring," in *Proc. Eur. Conf. Comp. Vis. (ECCV)*. Cham, Switzerland: Springer, 2020, pp. 598–613.

[27] Y. Chang, H. Fang, L. Yan, and H. Liu, "Joint blind deblurring and destriping for remote sensing images," in *Proc. IEEE Int. Conf. Image Process.*, Sep. 2013, pp. 469–473.

[28] L. Bar, N. Sochen, and N. Kiryati, "Semi-blind image restoration via Mumford–Shah regularization," *IEEE Trans. Image Process.*, vol. 15, no. 2, pp. 483–493, Feb. 2006.

[29] Y. Chang, L. Yan, B. Chen, S. Zhong, and Y. Tian, "Hyperspectral image restoration: Where does the low-rank property exist," *IEEE Trans. Geosci. Remote Sens.*, vol. 59, no. 8, pp. 6869–6884, Aug. 2020.

[30] A. H. Lettington, S. Tzimopoulou, and M. P. Rollason, "Nonuniformity correction and restoration of passive millimeter-wave images," *Opt. Eng.*, vol. 40, no. 2, pp. 268–274, 2001.

Authorized licensed use limited to: XIDIAN UNIVERSITY. Downloaded on November 24,2022 at 09:16:45 UTC from IEEE Xplore. Restrictions apply.

[31] Y. Chang, L. Yan, M. Chen, H. Fang, and S. Zhong, "Two-stage convolutional neural network for medical noise removal via image decomposition," *IEEE Trans. Instrum. Meas.*, vol. 69, no. 6, pp. 2707–2721, Jun. 2019.

[32] R. Srinivasan, M. Cannon, and J. White, "Landsat data destriping using power spectral filtering," *Opt. Eng.*, vol. 27, no. 11, Nov. 1988, Art. no. 271193.

[33] B. Münch, P. Trtik, F. Marone, and M. Stampanoni, "Stripe and ring artifact removal with combined wavelet-Fourier filtering," *Opt. Exp.*, vol. 17, no. 10, pp. 8567–8591, 2009.

[34] R. Pande-Chhetri and A. Abd-Elrahman, "De-striping hyperspectral imagery using wavelet transform and adaptive frequency domain filtering," *ISPRS J. Photogramm. Remote Sens.*, vol. 66, no. 5, pp. 620–636, Sep. 2011.

[35] H. Carfantan and J. Idier, "Statistical linear destriping of satellite-based pushbroom-type images," *IEEE Trans. Geosci. Remote Sens.*, vol. 48, no. 4, pp. 1860–1871, Apr. 2010.

[36] M. Bouali and S. Ladjal, "Toward optimal destriping of MODIS data using a unidirectional variational model," *IEEE Trans. Geosci. Remote Sens.*, vol. 49, no. 8, pp. 2924–2935, Apr. 2011.

[37] X. Lu, Y. Wang, and Y. Yuan, "Graph-regularized low-rank representation for destriping of hyperspectral images," *IEEE Trans. Geosci. Remote Sens.*, vol. 51, no. 7, pp. 4009–4018, Jul. 2013.

[38] Y. Chang, L. Yan, T. Wu, and S. Zhong, "Remote sensing image stripe noise removal: From image decomposition perspective," *IEEE Trans. Geosci. Remote Sens.*, vol. 54, no. 12, pp. 7018–7031, Dec. 2016.

[39] X. Liu, X. Lu, H. Shen, Q. Yuan, Y. Jiao, and L. Zhang, "Stripe noise separation and removal in remote sensing images by consideration of the global sparsity and local variational properties," *IEEE Trans. Geosci. Remote Sens.*, vol. 54, no. 5, pp. 3049–3060, May 2016.

[40] Y. Chen, T.-Z. Huang, L.-J. Deng, X.-L. Zhao, and M. Wang, "Group sparsity based regularization model for remote sensing image stripe noise removal," *Neurocomputing*, vol. 267, pp. 95–106, Dec. 2017.

[41] Y. Chen, T.-Z. Huang, and X.-L. Zhao, "Destriping of multispectral remote sensing image using low-rank tensor decomposition," *IEEE J. Sel. Topics Appl. Earth Observ. Remote Sens.*, vol. 11, no. 12, pp. 4950–4967, Dec. 2018.

[42] N. Liu, W. Li, R. Tao, and J. E. Fowler, "Wavelet-domain low-rank/group-sparse destriping for hyperspectral imagery," *IEEE Trans. Geosci. Remote Sens.*, vol. 57, no. 12, pp. 10310–10321, Dec. 2019.

[43] P. Xiao, Y. Guo, and P. Zhuang, "Removing stripe noise from infrared cloud images via deep convolutional networks," *IEEE Photon. J.*, vol. 10, no. 4, pp. 1–14, Aug. 2018.

[44] Y. Zhong, W. Li, X. Wang, S. Jin, and L. Zhang, "Satellite-ground integrated destriping network: A new perspective for EO-1 hyperion and Chinese hyperspectral satellite datasets," *Remote Sens. Environ.*, vol. 237, Feb. 2020, Art. no. 111416.

[45] Z. Hu and M.-H. Yang, "Learning good regions to deblur images," *Int. J. Comput. Vis.*, vol. 115, no. 3, pp. 345–362, 2015.

[46] Z. Hu and M.-H. Yang, "Good regions to deblur," in *Proc. Eur. Conf. Comp. Vis. (ECCV)*. Cham, Switzerland: Springer, 2012, pp. 59–72.

[47] J. Sun, W. Cao, Z. Xu, and J. Ponce, "Learning a convolutional neural network for non-uniform motion blur removal," in *Proc. IEEE Conf. Comput. Vis. Pattern Recognit. (CVPR)*, Jun. 2015, pp. 769–777.

[48] O. Kupyn, V. Budzan, M. Mykhailych, D. Mishkin, and J. Matas, "DeblurGAN: Blind motion deblurring using conditional adversarial networks," in *Proc. IEEE/CVF Conf. Comput. Vis. Pattern Recognit.*, Jun. 2018, pp. 8183–8192.

[49] O. Kupyn, T. Martyniuk, J. Wu, and Z. Wang, "DeblurGAN-v2: Deblurring (orders-of-magnitude) faster and better," in *Proc. IEEE/CVF Int. Conf. Comput. Vis. (ICCV)*, Oct. 2019, pp. 8878–8887.

[50] X.-L. Zhao, F. Wang, T.-Z. Huang, M. K. Ng, and R. J. Plemmons, "Deblurring and sparse unmixing for hyperspectral images," *IEEE Trans. Geosci. Remote Sens.*, vol. 51, no. 7, pp. 4045–4058, Jul. 2013.

[51] H. Shen, W. Zhao, Q. Yuan, and L. Zhang, "Blind restoration of remote sensing images by a combination of automatic knife-edge detection and alternating minimization," *Remote Sens.*, vol. 6, no. 8, pp. 7491–7521, Aug. 2014.

[52] H. Lim, S. Yu, K. Park, D. Seo, and J. Paik, "Texture-aware deblurring for remote sensing images using l_0-based deblurring and l_2-based fusion," *IEEE J. Sel. Topics Appl. Earth Observ. Remote Sens.*, vol. 13, pp. 3094–3108, 2020.

[53] Z. Zhang *et al.*, "Blind remote sensing image deblurring using local binary pattern prior," *Remote Sens.*, vol. 14, no. 5, p. 1276, Mar. 2022.

[54] P. Zhang, J. Li, E. Olson, T. J. Schmit, J. Li, and W. P. Menzel, "Impact of point spread function on infrared radiances from geostationary Satellites," *IEEE Trans. Geosci. Remote Sens.*, vol. 44, no. 8, pp. 2176–2183, Aug. 2006.

[55] D. Serre *et al.*, "Modeling the spatial PSF at the VLT focal plane for muse WFM data analysis purpose," in *Proc. SPIE*, vol. 7736, 2010, Art. no. 773649.

[56] S. Cao, W. Tan, K. Xing, H. He, and J. Jiang, "Dark channel inspired deblurring method for remote sensing image," *J. Appl. Remote Sens.*, vol. 12, no. 1, Feb. 2018, Art. no. 015012.

[57] Y. Chang, L. Yan, X. Zhao, H. Fang, Z. Zhang, and S. Zhong, "Weighted low-rank tensor recovery for hyperspectral image restoration," *IEEE Trans. Cybern.*, vol. 50, no. 11, pp. 4558–4572, Nov. 2020.

[58] D. Hong *et al.*, "More diverse means better: Multimodal deep learning meets remote-sensing imagery classification," *IEEE Trans. Geosci. Remote Sens.*, vol. 59, no. 5, pp. 4340–4354, Aug. 2020.

[59] D. Hong, L. Gao, J. Yao, B. Zhang, A. Plaza, and J. Chanussot, "Graph convolutional networks for hyperspectral image classification," *IEEE Trans. Geosci. Remote Sens.*, vol. 59, no. 7, pp. 5966–5978, Jul. 2020.

[60] X. Wu, D. Hong, and J. Chanussot, "Convolutional neural networks for multimodal remote sensing data classification," *IEEE Trans. Geosci. Remote Sens.*, vol. 60, pp. 1–10, 2021.

[61] A. Maffei, J. M. Haut, M. E. Paoletti, J. Plaza, L. Bruzzone, and A. Plaza, "A single model CNN for hyperspectral image denoising," *IEEE Trans. Geosci. Remote Sens.*, vol. 58, no. 4, pp. 2516–2529, Apr. 2019.

[62] Q. Yuan, Q. Zhang, J. Li, H. Shen, and L. Zhang, "Hyperspectral image denoising employing a spatial–spectral deep residual convolutional neural network," *IEEE Trans. Geosci. Remote Sens.*, vol. 57, no. 2, pp. 1205–1218, Sep. 2018.

[63] Y. Chang, L. Yan, and W. Liao, "HSI-DeNet: Hyperspectral image restoration via convolutional neural network," *IEEE Trans. Geosci. Remote Sens.*, vol. 57, no. 2, pp. 667–682, Feb. 2018.

[64] X. Cao, X. Fu, C. Xu, and D. Meng, "Deep spatial–spectral global reasoning network for hyperspectral image denoising," *IEEE Trans. Geosci. Remote Sens.*, vol. 60, pp. 1–14, 2021.

[65] Y. Bai, G. Cheung, X. Liu, and W. Gao, "Graph-based blind image deblurring from a single photograph," *IEEE Trans. Image Process.*, vol. 28, no. 3, pp. 1404–1418, Mar. 2018.

[66] J. Dong and J. Pan, "Deep outlier handling for image deblurring," *IEEE Trans. Image Process.*, vol. 30, pp. 1799–1811, 2021.

[67] L. Chen, J. Zhang, S. Lin, F. Fang, and J. S. Ren, "Blind deblurring for saturated images," in *Proc. IEEE/CVF Conf. Comput. Vis. Pattern Recognit. (CVPR)*, Jun. 2021, pp. 6308–6316.

[68] J. Wright, A. Ganesh, S. Rao, and Y. Ma, "Robust principal component analysis: Exact recovery of corrupted low-rank matrices via convex optimization," in *Proc. Adv. Neural Inf. Process. Syst.*, Dec. 2009, vol. 58, no. 3, pp. 289–298.

[69] S. D. Babacan, R. Molina, and A. K. Katsaggelos, "Variational Bayesian blind deconvolution using a total variation prior," *IEEE Trans. Image Process.*, vol. 18, no. 1, pp. 12–26, Jan. 2008.

[70] T. Goldstein and S. Osher, "The split Bregman method for L1-regularized problems," *SIAM J. Imag. Sci.*, vol. 2, no. 2, pp. 323–343, 2009.

[71] L. Xu, C. Lu, Y. Xu, and J. Jia, "Image smoothing via L_0 gradient minimization," in *Proc. SIGGRAPH ASIA Conf.*, 2011, pp. 1–12.

[72] H. Ji and K. Wang, "Robust image deblurring with an inaccurate blur kernel," *IEEE Trans. Image Process.*, vol. 21, no. 4, pp. 1624–1634, Apr. 2011.

[73] K. Zhang, W. Zuo, Y. Chen, D. Meng, and L. Zhang, "Beyond a Gaussian denoiser: Residual learning of deep CNN for image denoising," *IEEE Trans. Image Process.*, vol. 26, no. 7, pp. 3142–3155, Jul. 2017.

[74] B. Zhou, A. Lapedriza, A. Khosla, A. Oliva, and A. Torralba, "Places: A 10 million image database for scene recognition," *IEEE Trans. Pattern Anal. Mach. Intell.*, vol. 40, no. 6, pp. 1452–1464, Jun. 2017.

[75] D. Krishnan and R. Fergus, "Fast image deconvolution using hyper-Laplacian priors," in *Proc. Adv. Neural Inf. Process. Syst.*, vol. 22, 2009, pp. 1033–1041.

[76] J.-F. Cai, H. Ji, C. Liu, and Z. Shen, "Framelet-based blind motion deblurring from a single image," *IEEE Trans. Image Process.*, vol. 21, no. 2, pp. 562–572, Feb. 2011.

[77] J.-F. Cai, S. Osher, and Z. Shen, "Split Bregman methods and frame based image restoration," *Multiscale Model. Simul.*, vol. 8, no. 2, pp. 337–369, 2010.

[78] J.-F. Cai, E. J. Candès, and Z. Shen, "A singular value thresholding algorithm for matrix completion," *SIAM J. Optim.*, vol. 20, no. 4, pp. 1956–1982, Mar. 2010.

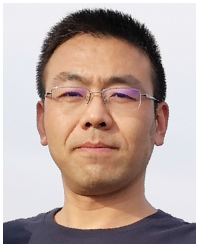
Authorized licensed use limited to: XIDIAN UNIVERSITY. Downloaded on November 24,2022 at 09:16:45 UTC from IEEE Xplore. Restrictions apply.

[79] J.-Y. Zhu, T. Park, P. Isola, and A. A. Efros, "Unpaired image-to-image translation using cycle-consistent adversarial networks," in *Proc. IEEE Conf. Comput. Vis. Pattern Recognit. (CVPR)*, Oct. 2017, pp. 2223–2232.
[80] S. W. Zamir *et al.*, "Multi-stage progressive image restoration," in *Proc. IEEE/CVF Conf. Comput. Vis. Pattern Recognit. (CVPR)*, Jun. 2021, pp. 14821–14831.
[81] Z. Wang, A. C. Bovik, H. R. Sheikh, and E. P. Simoncelli, "Image quality assessment: From error visibility to structural similarity," *IEEE Trans. Image Process.*, vol. 13, no. 4, pp. 600–612, Apr. 2004.
[82] D. Hong, N. Yokoya, J. Chanussot, and X. X. Zhu, "An augmented linear mixing model to address spectral variability for hyperspectral unmixing," *IEEE Trans. Image Process.*, vol. 28, no. 4, pp. 1923–1938, Apr. 2018.



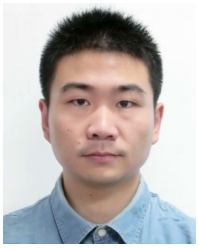
Shuning Cao received the B.S. degree in control engineering from the Huazhong University of Science and Technology (HUST), Wuhan, China, in 2018, where he is currently pursuing the Ph.D. degree with the School of Artificial Intelligence and Automation.

His research interests include image deblurring, structural noise removal, and multispectral image processing.



Houzhang Fang (Member, IEEE) received the Ph.D. degree in control science and engineering from the Huazhong University of Science and Technology, Wuhan, China, in 2014.

He is currently an Associate Professor with the School of Computer Science and Technology, Xidian University, Xi'an, China. His research interests include target recognition and image restoration.



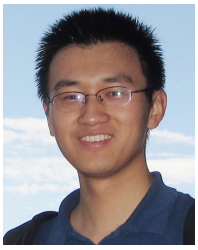
Liqun Chen received the B.S. degree from the School of Materials Science and Engineering, Huazhong University of Science and Technology (HUST), Wuhan, China, in 2012, and the Ph.D. degree from the School of Artificial Intelligence and Automation, HUST, in 2019.

He currently holds a post-doctoral position at the School of Artificial Intelligence and Automation, HUST. His research interests include computer vision and image processing, in particular, embedded image processing system.



Wei Zhang received the B.S. degree in measurement technology and instrumentation and the Ph.D. degree in instrument science and technology from Chongqing University, Chongqing, China, in 2012 and 2016, respectively.

From 2017 to 2020, he was a Post-Doctoral Fellow with the College of Optoelectronic Engineering, Chongqing University. He is currently an Assistant Researcher with the Artificial Intelligence Center, Peng Cheng Laboratory, Shenzhen, China. His research interests include optical fiber sensing, radar/LiDAR, image processing, neuromorphic vision, and optimization.



Yi Chang (Member, IEEE) received the B.S. degree in automation from the University of Electronic Science and Technology of China, Chengdu, China, in 2011, and the M.S. degree in pattern recognition and intelligent systems and the Ph.D. degree in control science and engineering from the Huazhong University of Science and Technology (HUST), Wuhan, China, in 2014 and 2019, respectively.

From 2014 to 2015, he was a Research Assistant with Peking University, Beijing, China. From 2019 to 2021, he was a Post-Doctoral Researcher with Peng Cheng Laboratory, Shenzhen, China. He is currently a Lecturer with the School of Artificial Intelligence and Automation, HUST. His research interests include image processing, computer vision, and machine learning.



Luxin Yan (Member, IEEE) received the B.S. degree in electronic communication engineering and the Ph.D. degree in pattern recognition and intelligence system from the Huazhong University of Science and Technology (HUST), Wuhan, China, in 2001 and 2007, respectively.

He is currently a Professor with the School of Artificial Intelligence and Automation, HUST. His research interests include multispectral image processing, pattern recognition, and real-time embedded system.

Authorized licensed use limited to: XIDIAN UNIVERSITY. Downloaded on November 24,2022 at 09:16:45 UTC from IEEE Xplore. Restrictions apply.